A neurite-zippering mechanism, mediated by layer-specific expression of IgCAMs, regulates synaptic laminar specificity in the *C. elegans* nerve ring neuropil

Authors: Titas Sengupta[1], Noelle L. Koonce[1], Mark W. Moyle[1], Leighton H. Duncan[1], Nabor Vázquez-Martínez[1], Xiaofei Han[2], Lin Shao[1], Yicong Wu[2], Anthony Santella[3], Li Fan[3], Zhirong Bao[3], William A. Mohler[5], Hari Shroff[2, 4], Daniel A. Colón-Ramos[1, 4, 6*]

Affiliations:

1. Department of Neuroscience and Department of Cell Biology, Yale University School of Medicine, New Haven, CT 06536, USA.

2. Laboratory of High Resolution Optical Imaging, National Institute of Biomedical Imaging and Bioengineering, National Institutes of Health, Bethesda, MD 20892, USA.

3. Developmental Biology Program, Sloan Kettering Institute, New York, NY 10065, USA.

4. MBL Fellows, Marine Biological Laboratory, Woods Hole, MA 02543, USA

5. Department of Genetics and Genome Sciences and Center for Cell Analysis and Modeling, University of Connecticut Health Center, Farmington, CT 06030, USA.

6. Instituto de Neurobiología, Recinto de Ciencias Médicas, Universidad de Puerto Rico, San Juan 00901, Puerto Rico. 56

*Correspondence to:

Daniel A. Colón-Ramos, Ph.D.
Department of Neuroscience
Department of Cell Biology
Yale University School of Medicine
333 Cedar Street
SHM B 163D
New Haven, CT 06510
Email: daniel.colon-ramos@yale.edu

Abstract

A fundamental design principle of nervous systems is the grouping of neuronal contacts into layers within nerve bundles. The layered arrangement of neurites requires nanoscale precision in their placement within bundles, and this precision, which can not be exclusively explained by simple tip-directed outgrowth dynamics, underpins synaptic specificity and circuit architecture. Here we implement novel imaging methods and deep learning approaches to document the specific placement of single neurites during the assembly of the *C. elegans* nerve ring. We uncover a zippering mechanism that controls precise placement of neurites onto specific layer subdomains. Nanoscale precision in neurite placement is orchestrated via temporally-regulated expression of specific Ig adhesion molecules, such as SYG-1. Ig adhesion molecules act as instructive signals, defining sublaminar regions and guiding neurite zippering onto target neurons. Our study reveals novel developmental mechanisms that coordinate neurite placement and synaptic specificity within layered brain structures.

Introduction

In brains, neurites are segregated away from the cell bodies into synapse-rich regions termed neuropils: dense structures of nerve cell extensions which commingle to form functional circuits (Maynard, 1962). Neuropils are units of functional organization within brains, and within the precisely arranged architecture of the neuropil, placement of neurites into specific neighborhoods is a major determinant of synaptic specificity and circuit connectivity (Maynard, 1962; Schürmann, 2016; Soiza-Reilly & Commons, 2014; Xu et al., 2020; Zheng et al., 2018). Proper functional connectivity therefore depends on design principles that guide placement of neurites, at nanoscale precision, within neuropils.

A fundamental design principle of neuropil organization is the segregation of neurites into laminae and sublaminae, and this laminar organization principle is conserved and observed in neuropils of both vertebrate and invertebrates (Gabriel et al., 2012; Millard & Pecot, 2018; Sanes & Zipursky, 2010). The laminar structural organization is key to the assembly and functional segregation of specific circuits (Gabriel et al., 2012; Kolodkin & Hiesinger, 2017; Millard & Pecot, 2018; Nevin et al., 2008). For example, in the inner plexiform layer (IPL) of the vertebrate retina, synaptic connections conveying different types of visual information spatially segregate onto distinct sublayers. Placement of neurites with similar functions into specific sublayers restricts synaptic partner choice, driving synaptic specificity (Robles et al., 2013). Therefore, the co-segregation of neurons with similar response properties into specific layers gives rise to topographic maps in which structural principles underpin functional

73 principles in the precise assembly, and segregation, of distinct circuits (Clandinin &
74 Feldheim, 2009).

75 Within the layered organization of neuropils, subsets of neurons are capable of
76 specifically projecting onto multiple layers, enabling integration of information across
77 laminar circuits. For example, glycinergic and GABAergic amacrine cells in the IPL of
78 the retina, and the periventricular projection neurons in the zebrafish tectal neuropil,
79 extend single neurites that link multiple sublayers within their respective neuropils
80 (Demb & Singer, 2012; Kolb, 1995; Kunzevitzky et al., 2013; Robles et al., 2011; Strettoi
81 et al., 1992; Taylor & Smith, 2012). Their precise placement, and the distribution of
82 synapses within neurite regions, underlies their functional roles as integrators of
83 information across the modular and layered circuit architecture (Robles et al., 2011;
84 Strettoi et al., 1992; Taylor & Smith, 2012). How the precise placement of these
85 multilayer-spanning neurites is specified during development, particularly in the context
86 of the assembling neuropil, is not understood.

87 Molecular genetic studies have revealed roles for cell adhesion molecules
88 (CAMs) and guidance factors in neuronal targeting onto specific layers of the brain. For
89 example, studies in both the mouse and fly visual systems have revealed important
90 roles for IgSF proteins, such as the Sidekick, Dscam and Contactin molecules, in
91 targeting neurons to distinct layers or sublaminae (Sanes & Zipursky, 2020; Tan et al.,
92 2015; Yamagata & Sanes, 2008, 2012). These studies indicate that the expression
93 levels, the timing of expression and the co-expression of specific CAMs influence layer-
94 specific targeting of neurites within neuropils (Petrovic & Hummel, 2008a; Poskanzer et
95 al., 2003; Schwabe et al., 2014). These observations also reveal that our current

mechanistic frameworks of axon guidance and cell-cell interactions are insufficient to provide a conceptual understanding of how nanoscale organization within neuropils emerges during development. In particular, how single cells make simultaneous and coordinated use of these molecular cues to achieve precise placement, resulting in synaptic specificity within layered neuropils, is poorly understood.

The *C. elegans* nerve ring is a crowded neuropil tens of micrometers thick in which neuronal processes have to discriminate between targets to assemble functional circuits that underpin specific behaviors (Ware et al., 1975; White et al., 1986). We recently demonstrated that the *C. elegans* nerve ring neuropil is a layered structure, with layers (called “strata”) that functionally segregate sensory information and motor outputs (Moyle et al., 2020). A subset of highly interconnected neurons, which form part of a group called ‘rich-club neurons’, serve as hubs that link functionally distinct strata, analogous to amacrine cells in the inner plexiform layer of the vertebrate retina (Marc et al., 2014; Moyle et al., 2020; Towlson et al., 2013). The precise placement of these rich-club neurons along distinct nerve ring strata, and the specific segregation of their synaptic inputs and outputs between these strata, are important for supporting the structure and function of the nematode brain (Gray et al., 2005; Moyle et al., 2020; Wakabayashi et al., 2004).

To determine how neuronal processes are precisely placed onto specific layers during development, and the implications of this placement for synaptic connectivity, we examined the AIB interneurons, a pair of “rich-club neurons” that integrate sensory and motor information across nerve ring strata (Chalasani et al., 2007; Kang & Avery, 2009; Moyle et al., 2020; Sabrin et al., 2019; Towlson et al., 2013). Each AIB neuron projects

a single neurite, and segments of that single neurite are placed along distinct and specific layers in the *C. elegans* nerve ring. The nanoscale precision of AIB neurite placement informs the specificity of AIB synaptic sites in the dense neuropil structure of the nerve ring.

We labeled the AIB neurons for visualization *in vivo* and implemented novel imaging methods and deep learning approaches to yield high-resolution images of AIB during embryonic development. We discovered that placement of the AIB neurite depends on coordinated zippering mechanisms that align segments of the AIB neurite onto specific sublayers. Through forward and reverse genetic screens we uncovered molecular factors important for placement of the AIB neurite. We identified roles for the IgCAM *syg-1* in zippering a segment of the AIB neurite onto a layer boundary. We determined that *syg-1* expression is layer specific, and temporally controlled to coincide with AIB neurite outgrowth and zippering onto the correct sublayer. Expression of SYG-1 is sufficient to specify AIB neurite placement, and ectopic expression of just the SYG-1 ectodomain results in segments of the AIB neurite being incorrectly positioned at the ectopic SYG-1-expressing layers. Our findings uncover a novel zippering mechanism which acts *in vivo* to place neurites along specific layers of the nerve ring neuropil. This mechanism is based on a temporally-coordinated expression of IgCAMs at specific layer subdomains. The developmental processes uncovered in this *in vivo* study might represent conserved mechanisms that enable placement of neurites, and *en passant* synaptic specificity, in layered neuropil structures.

Results

The AIB neurites are placed along distinct strata in the *C. elegans* nerve ring neuropil

To characterize the precise placement and synaptic distribution of the AIB neurites in the context of the nerve ring neuropil strata, we examined available connectome datasets generated across the larval developmental stages of *C. elegans*(White et al., 1986; Witvliet et al., 2020). Synapses in AIB, like in most nerve ring neurons, are formed *en passant*, or along the length of its single neurite. AIB displays polarity in the distribution of its synaptic specializations: postsynaptic specializations are enriched in the proximal neurite (near the cell body), while presynaptic specializations are enriched in the distal neurite (Fig. 1a-c). Examination of the connectomes revealed that the synaptic polarity of AIB is stereotyped, established by the L1 stage and preserved throughout development (Witvliet et al., 2020)(https://nemanode.org/).

Segments of the AIB single neurite reside along distinct strata of the nerve ring (Supplementary Fig. 1a). The AIB proximal neurite, which is enriched in postsynaptic specializations, forms contacts with neighboring amphid sensory neurons in a sub-bundle coincident with S3/S4 sublaminar region, hereafter termed 'AIB proximal neighborhood'. The AIB distal neurite, which is enriched in presynaptic specializations, contacts neighboring motor interneurons in a sub-bundle coincident with S2/S3 sublaminar region, hereafter termed 'AIB distal neighborhood'. In the distal neighborhood, the highest number of AIB contacts are formed with the neurites of motor neuron RIM (Supplementary Fig. 1b,c), a major fasciculation partner and postsynaptic

partner of AIB, located at the S2/S3 sublaminar region (Supplementary Fig. 1b). In the proximal neighborhood, AIB receives synaptic inputs from sensory neurons in the S3/4 sublaminar region (Supplementary Fig. 1b,d). Therefore, placement of the AIB neurite onto these distinct neighborhoods links sensory information (from the S3/4 sublaminar region) to motor neuron outputs (in the S2/S3 sublaminar region) in the nerve ring neuropil. This design principle of the AIB neurite is present in early larval stages and preserved upto adulthood (Supplementary Fig. 1b)(Witvliet et al., 2020).

The AIB neurite segments reach the proximal and distal neighborhoods via a shift of the neurite along the anteroposterior axis, precisely at the dorsal mid-line of the nerve ring (herein refered to as the “chiasm”, as the shift results in a cross-over of the two AIB neurites; indicated by arrowheads in Fig.1a-g, Supplementary Fig. 1e-j). Remarkably, the shift of the AIB neurite is precisely the width of the S3 strata, enabling it to bridge the S3/4 and S2/3 sublaminae with the positioning of its neurite segments (Supplementary Fig. 1). Network analyses on the contacts of AIBL and AIBR with other neurons across the available connectomes revealed similarity in number and distribution of AIB contacts across development (pairwise cosine similarity index S, ranges from 0.62-0.97, $S>0.5$ representing a positive correlation between datasets, Supplementary Fig. 2a-c also see Methods). This is indicative of a developmental program that establishes contact profiles for AIB during embryogenesis, and is allosterically maintained during post-embryonic growth (Fan et al., 2020). We also found that AIBL and AIBR have high betweenness centrality (a standard property for rich-club neurons (Towlson et al., 2013)) in an L1 (first larval stage after embryogenesis) and an adult connectome dataset (Witvliet et al., 2020), suggesting that AIB functions as a rich

188 club neuron at early as well as later postembryonic developmental stages
189 (Supplementary Fig. 2d). Moreover, examination of AIB in the connectome of the
190 nematode *Pristionchus pacificus,* which is separated from *C. elegans* by 100 million
191 years of evolutionary time, revealed similar design principles in morphology and
192 placement of the AIB neurite (Hong et al., 2019). Therefore AIB morphology, position
193 and polarity are conserved features of the architecture of the nematode brain,
194 established during embryonic development and are uniquely designed to integrate and
195 relay information across functional modules of the nerve ring. The developmental
196 programs that govern these design principles, enabling nanoscale precision in the
197 placement of the AIB neurite onto specific neighborhoods and the segregation of
198 synaptic specializations, are not understood.
199
200 **_In vivo_ visualization of AIB synaptic distribution and placement in the nerve**
201 **ring neuropil**
202 To examine the developmental programs of AIB, we developed cellular and
203 subcellular fluorescent labels for imaging of AIB, its neighborhoods and its synapses *in*
204 *vivo* in embryonic stages and postembryonic larval stages. The synaptic distribution that
205 we observed by fluorescent labeling was consistent with the EM connectomic
206 characterizations: presynaptic proteins RAB-3 and CLA-1 localized exclusively to the
207 distal segment of the neurite, while postsynaptic protein GLR-1 localized primarily to the
208 proximal neurite segment (Fig. 1d,e; Polarity index, PI = 0.92 for RAB-3 and 0.24 for
209 GLR-1, where PI>0.5 represents a distal localization and PI<0.5 represents a proximal
210 localization). These markers also enable visualization of the chiasm that result in the

separation of the two AIB neurite segments onto distinct neighborhoods along the antero-posterior axis of the worm (Fig. 1f-l, Supplementary Fig. 1g,h). We found that the chiasm is stereotyped and similar in length across L4 stage animals, as measured from confocal micrographs (mean length = 2.97±0.22 μm, number of neurons measured, n =22), and electron micrographs (dorsal midline shift length in AIBL and AIBR in electron micrographs of an L4 stage animal, JSH, are 3.01 μm and 3.16 μm respectively).

To visualize the AIB neurite in the context of the proximal and distal neighborhoods, we co-labeled neurons that extensively contact (fasciculate) with AIB in the proximal and distal neighborhoods: motor neuron RIM for the distal neighborhood and sensory neurons AWC and ASE for the proximal neighborhood (Supplementary Fig. 1c,d). Consistent with the EM connectomic studies, these representative neighborhood markers overlap with the expected neighborhoods (Fig. 1f-m). Our findings are consistent with and extend previous studies, demonstrating that the AIB unique morphology emerges early in development, is stereotyped across animals and is conserved throughout evolution (Hong et al., 2019; White et al., 1983). Our examination of AIB in the context of electron micrographs from connectomic studies and *in vivo* imaging reveal that the AIB neurite is designed, by its position and distribution of synapses, to occupy distinct neighborhoods and integrate information across strata of the nerve ring.

Modular developmental programs underlie precise placement and synaptic polarity of the AIB neurites

To understand the cellular and molecular mechanisms underpinning the precise placement of the AIB neurites in the context of the nerve ring neuropil, and how their placement relates to synaptic polarity, we performed unbiased forward genetic screens and candidate screens in postembryonic larval stage animals. Our screens uncovered mutants with defects in AIB neurite outgrowth and placement: a novel mutant allele of transcription factor *daf-16*/FOXO (*ola337*) (Supplementary Table 1), lesions in genes encoding cytoskeletal regulators (*unc-33 and zyg*-8) and lesions in axon guidance genes (*vab-1*, *unc-6* and *sax-3)*. These mutants result in defects in AIB neurite placement in the context of the neighborhoods by affecting AIB outgrowth and/or nerve ring neighborhood development (Fig. 2; Supplementary Fig. 3), (Christensen et al., 2011; Grossman et al., 2013; Yoshimura et al., 2008; Zallen et al., 1999)). Interestingly, inspection of AIB subcellular distribution of pre- and postsynaptic specializations in these mutant backgrounds revealed that when AIB morphology and the nerve ring neighborhoods are affected, the AIB neurites still exhibit a polarized distribution of pre- and postsynaptic proteins (Fig. 2). For instance, even in cases in which the distal AIB neurite segment was largely absent, the neurite retained the polarized distribution of pre and postsynaptic proteins, with presynaptic components accumulating specifically in the distal segment, or tip, of the truncated neurite and not in the proximal neurite (Fig. 2e-l). The retainment of synaptic polarity even in extreme cases of neurite outgrowth or neighborhood placement defects suggests modularity between the developmental

processes dictating neurite placement and the polarized distribution of pre- and postsynaptic specializations in the context of the proximal and distal neurite segments.

Our genetic findings suggest that synaptic specificity in AIB requires the correct deployment of two modular developmental programs: polarized placement of pre- and postsynaptic specializations along the neurite, and the placement of the neurite onto the correct strata. To specifically understand the mechanisms that regulate placement of the AIB neurite onto the correct strata, we focused our analyses on mutants with nanoscale defects in the placement of the AIB neurite within specific neighborhoods.

The IgCAM SYG-1 is required for precise placement of the AIB distal neurite in the nerve ring

From our screens we discovered that loss-of-function mutant alleles of the Ig superfamily CAM gene *syg-1* result in significant defects in placement of the AIB neurite in the nerve ring. In wild type animals, we observed overlap between the AIB distal neurite, and its distal neighborhood partner, RIM (Fig. 3a-d), consistent with electron microscopy characterizations of AIB and RIM fasciculation (Supplementary Fig. 1b). In contrast, in *syg-1* mutants the AIB neurites are frequently detached or separated from the RIM neurites (Fig. 3e-h). 70.7% of *syg-1(ky652)* animals and 62.5% of *syg-1(ok3640)* animals (as compared to 0% of wild type animals) show regions of AIB-RIM detachment, i.e., failure of the AIB and RIM neurites to fasciculate along their entire length in the distal neighborhood. Cosmid C54A10, containing the *syg-1* genomic region, rescued the distal neurite placement defects in *syg-1(ky652)* (in 87.5% of animals with the rescuing construct, the AIB and RIM neurites show complete overlap

as in wild type animals) (Fig. 3i-l). In the *syg-1(ky652)* animals that exhibit defects in AIB neurite placement with respect to RIM, we calculated the percentage of AIB-RIM neurite contact length that exhibits detachment or separation, and found the average percent detachment to be 21.49±4% of total contact length in *syg-1(ky652)* mutant animals (Fig. 1m, also see Methods). The AIB chiasm is also significantly reduced in length in *syg-1* mutants (Supplementary Fig. 4a), and the distal neurite is not positioned at a uniform distance from the proximal AIB neurite (Fig. 1n), consistent with a placement defect of the AIB distal neurite onto the distal neighborhood . We note that in the *syg-1(ky652)* mutant animals, the cell body position of AIB, AIB's neurite length and placement of the AIB proximal neurite segment are unaffected (Supplementary Fig. 4b,c), suggesting that *syg-1* specifically regulates the placement of the distal neurite segment in the distal neighborhood. Our findings indicate that correct placement of the AIB proximal neurite and the distal neurite are genetically separable. Importantly, our findings indicate that Ig superfamily cell adhesion molecule SYG-1 is necessary for nanoscale placement of the AIB neurite to the distal nerve ring neighborhood.

SYG-1 and its orthologs (Rst and Kirre in *Drosophila* and Kirrel1/2/3 in mammals) are multipurpose adhesion molecules which function in a wide variety of developmental contexts, including synapse formation in the *C. elegans* egg-laying circuit, muscle cell fusion, eye patterning and olfactory axon convergence in *Drosophila*, and formation of the kidney filtration barrier in mammals (S. Bao & Cagan, 2005; Garg et al., 2007; Kim et al., 2015; Serizawa et al., 2006; Shen & Bargmann, 2003; ztokatli et al., 2012). Given SYG-1's known role in synaptogenesis in *C. elegans*, we examined the distribution of synaptic sites along the AIB distal neurite in *syg-1* mutants. We noted reduction in RAB-

3 signal in regions of the AIB distal neurite, but specifically for areas lacking RIM contacts (Supplementary Fig. 4g-p). We hypothesized that SYG-1 could mediate synaptogenesis in AIB, and that synapses might then help place AIB in the distal neighborhood. To test this hypothesis we identified, from our forward and reverse genetic screens, additional lesions resulting in synaptogenesis defects in AIB, including a novel allele of *syd-2(ola341)* (Supplementary Table 1), and *cla-1(ok560)* (Barstead et al., 2012; Xuan et al., 2017; Zhen & Jin, 1999). We observed that while *syd-2* and *cla-1* mutants result in an abnormal distribution of presynaptic specializations in AIB (Supplementary Fig. 4q-t), they do not display phenotypes in AIB neurite placement within the distal neighborhood (Supplementary Fig. 4u). Our findings indicate that molecules that affect synaptogenesis do not necessarily result in fasciulation defects for AIB. Together, our findings suggest that SYG-1 plays a role in mediating neurite placement specifically onto the distal neighborhood via fasciculation.

RIM neurons express SYG-1 and regulate AIB neurite placement

To understand how *syg-1* regulates the precise placement of the AIB neurite in its distal neighborhood, we next investigated where the *syg-1* gene is expressed. We achieved this by co-expressing an AIB reporter and a transcriptional reporter of *syg-1* (Schwarz et al., 2009) and examining its expression in the nerve ring of wild type animals. We observed robust expression of the *syg-1* transcriptional reporter in a banded pattern in the nerve ring neuropil, with specific enrichment in the AIB proximal and distal neighborhoods (Fig. 4a-d). By quantifying the ratio of mean intensities of the *syg-1* reporter in the proximal and distal neighborhoods, we found that on average, *syg-*

1 expression levels were 3.37 times (S.E.M. = 0.12) higher in the distal neighborhood relative to the proximal neighborhood (Fig. 4i). We then tested whether RIM, the primary distal neighborhood fasciculaton partner of AIB, expresses *syg-1*. Indeed, co-localization studies revealed *syg-1* reporter expression in RIM, but not in AIB, consistent with previous observations (Schwarz et al., 2009) (Fig. 4a-h). Therefore, neurons in the AIB distal nerve ring neighborhood, including RIM, express SYG-1.

As *syg-1* mutant animals exhibit defects in AIB neurite placement in the distal neighborhood, and as SYG-1 is expressed in RIM, we hypothesized that the RIM neurons might regulate placement of the AIB distal neurite onto the distal neighborhood. Via promoter screening and a systematic lineage tracing and cell identification pipeline (Z. Bao et al., 2006; Boyle et al., 2006; Duncan et al., 2019; Murray et al., 2006; Santella et al., 2014), we identified two promoters expressed in the RIM neurons prior to embryonic growth and placement of the AIB distal neurite (which occurs approximately 520-570 m.p.f. – see next section and Fig. 5). The promoters identified were *inx-19p* (expressed in RIM starting ~370 m.p.f (minutes post fertilization)) and *tdc-1p* (expressed in RIM starting ~445 m.p.f) (see Methods, Supplementary Fig. 5), http://promoters.wormguides.org). We then used these early promoters to drive an *in-vivo* split caspase ablation system (Chelur & Chalfie, 2007) to successfully eliminate the RIM neurons during embryogenesis (Supplementary Fig. 5d-g). Consistent with our hypothesis, we observed that ablation of RIM results in defects in placement of the AIB distal neurite to the distal neighborhood. These defects in RIM-ablated animals phenocopy the defects seen for the *syg-1* mutants. 80.6% and 51.5% of animals had defects in AIB distal neurite placement in RIM-ablated animals (using two strategies-

see Supplementary figure 5 and Methods), compared to 3.1% in a wild type population; Fig. 4j-q). These observations demonstrate that SYG-1-expressing RIM neurons are necessary for the precise placement of the AIB neurite in the distal neighborhood.

The AIB neurite is positioned in the distal neighborhood during embryonic development via a novel zippering mechanism

To understand how the RIM neurons contribute to placement of the AIB distal neurite segment, we examined the placement of the AIB and RIM neurites during embryogenesis. Imaging AIB and RIM in embryos required integration of subtractive labeling strategies for sparse labeling and *in vivo* tracking of the AIB neurites (Supplementary Fig. 6; Armenti et al., 2014a). It also required isotropic imaging via the use of dual-view light-sheet microscopy (diSPIM) (Kumar et al., 2014; Wu et al., 2013) and the development of a triple-view confocal microscope combined with a deep-learning framework for enhanced resolution ((Weigert et al., 2018; Wu et al., 2016),see details in Methods). Our high resolution and continuous imaging approaches in embryos revealed that the stereotypic placement of the AIB neurite involves **(a)** an initial phase of tip-directed outgrowth, and **(b)** relocation of part of the growing neurite to the distal neighborhood by a 'zippering' mechanism, as further described below.

(a) Initial tip-directed outgrowth: We observed that the cell bodies of the bilaterally symmetric AIB neurons display outgrowth of a neurite that enters the nerve ring ~ 400 m.p.f. The two AIB neurites then circumnavigate the nerve ring at opposite sides of the neuropil—with AIBL growing dorsally on the left side of the nerve ring, and AIBR also projecting dorsally, but at the right side of the ring (Fig. 5a,b). They grow along the

proximal neighborhood, fasciculating with the axons of amphid sensory neurons (from which they later receive synaptic inputs) (Supplementary Fig. 6d). The simultaneous outgrowth of the AIBL and AIBR neurons results in their neurites meeting at the dorsal midline of the nerve ring at approximately 460 m.p.f. The AIB outgrowth continues past their meeting point at the dorsal midline, and each AIB grows along each other, still along the proximal neighborhood, at 480 m.p.f. (Fig. 5c).

(b) Relocation to the distal neighborhood: We observed that around 500 m.p.f., the segment of each AIB neurite that has grown past the midline (ie, segment that will constitute the future distal neurite) starts separating from its lateral counterpart (the other AIB), starting from the growing tip (Fig. 5d-f, Supplementary Fig. 6e-g). The exit of the tip from the proximal neighborhood takes place as it extends straight, instead of following the ventral turn of the nerve ring, likely due to a loss of adhesion to proximal neighborhood neurons (Supplementary Fig. 6h,i). The growing tip then encounters the distal neighborhood (marked by RIM) at approximately 520 m.p.f. (Fig. 5h). Following this, the entire shaft of the future distal neurite relocates to the distal neighborhood, starting from the tip, and progressively ‘zippering’ towards the midline (Fig. 5i,j). At 510 minutes, 8% of the relocating distal neurite overlaps with RIM and the distal neighborhood. This overlap increases to 60% at around 535 mins and 96% at around 560 mins, demonstrating progressive overlap over time, analogous to the fastening of a zipper (see Methods). The separation or ‘unzippering’ from the proximal neighborhood and ‘zippering’ onto the distal neighborhood leads to repositioning of the entire distal neurite of AIB to a new neighborhood (Fig. 5j-n).

To investigate if placement of the AIB distal neurite by zippering has implications for synaptic protein distribution, we imaged presynaptic protein RAB-3 localization in the AIB distal neurite during the time when it is repositioned by zippering (520-570 m). We discovered that presynaptic proteins populate the neurite starting from the tip, progressively towards the dorsal midline in the same spatial pattern as AIB-RIM zippering-mediated contact (Supplementary Fig. 7). This suggests that the zippering mechanism might influence the spatiotemporal pattern of synaptic protein distribution in AIB upon contact with postsynaptic RIM. These findings are consistent with the observation in *syg-1(ky652)* that partial contact between AIB and RIM results in altered distribution of synaptic proteins to the sites of RIM contact.

Altogether, we discovered that the AIB neurite is positioned by a combination of tip-directed growth in the proximal neighborhood, circumferential exit of the distal neurite from the proximal neighborhood and its subsequent relocation and zippering to the distal neighborhood. The phenomenon of zippering of neurite shafts as a mechanism of fasciculation had been previously described in the context of dense primary neuron cultures (Barry et al., 2010; Šmít et al., 2017; Voyiadjis et al., 2011) but whether this occurs in developmental contexts *in vivo* is unknown. We demonstrate that the distal segment of the AIB neurite is placed in the correct neighborhood via a zippering mechanism onto a specific sublayer of the nerve ring.

Increase of local expression of SYG-1 at the distal neighborhood correlates with zippering of the distal AIB neurite onto its neighborhood

To understand how SYG-1 coordinates the developmental sequence of events that place the AIB neurite in specific neighborhoods, we examined the spatiotemporal dynamics of expression of the *syg-1* transcriptional reporter during embryogenesis. By long-term imaging using light sheet microscopy (diSPIM) we discovered that the *syg-1* promoter exhibits dynamic changes in spatial expression within nerve ring sublayers during the different events that occur to sequentially and precisely place the AIB neurite.

Similar to postembryonic animals, in embryos prior to hatching (~780 m.p.f.), the *syg-1* reporter is expressed in both proximal and distal AIB neighborhoods, with enrichment in the distal neighborhood (Fig. 6a-d). To investigate how this expression pattern emerges during development, we imaged the dynamics of expression of the *syg-1* promoter throughout the developmental period during which the AIB neurites are placed in the neighborhoods (400- 570 m.p.f.) (Fig. 5a-j). We observed:

1. Prior to 470 m.p.f., expression of the *syg-1* reporter in the nerve ring is primarily restricted to a single band corresponding to the AIB proximal neighborhood (Fig. 6e,i,i'). This coincides with periods of outgrowth by the AIBs in the proximal neighborhood.
2. Over the next two hours of embryogenesis (470-590 m.p.f.), a pair of neurons (one on each side of the nerve ring) robustly expressing *syg-1* grow into, and are placed in, the distal neighborhood (Fig. 6f,j,j'). Through colocalization studies we identified these pair of neurons to correspond to RIMs (Supplementary Fig. 8a-c). As RIMs grow into the distal neighborhood, we also observe the onset of *syg-1* expression in other distal neighborhood neurons (Fig. 6f-h). Therefore, during this period (470-590 m.p.f.) *syg-1*

437 expression levels increase in the distal neighborhood due to (a) ingrowth of the *syg-1*-
438 expressing RIM neurons into the neighborhood and (b) onset of *syg-1* expression in
439 other neurons in the neighborhood. This increase in *syg-1* expression in the distal
440 neighborhood is accompanied by a progressive decrease in *syg-1* levels in the proximal
441 neighborhood (Fig. 6j-l). Mean intensities of the *syg-1* reporter in the distal
442 neighborhood relative to the proximal neighborhood increases by 2-2.4 times (between
443 470-600 m.p.f; Supplementary Fig. 8d,e).

444 These observations indicate that dynamic changes in relative levels of *syg-1*
445 between specific nerve ring neighborhoods might underlie the specific placement of the
446 single AIB neurite across these neighborhoods. Altogether we provide evidence of
447 layered expression of an IgCAM in two specific nerve ring neighborhoods, observe that
448 the expression dynamically switches between these neighborhoods and describe how
449 these dynamic changes correlate with the nanoscale precise placement of a single
450 neurite (AIB) across these neighborhoods.

451

452 **Ectopic *syg-1* expression is sufficient to alter placement of the AIB distal**
453 **neurite**

454 To investigate if *syg-1* is instructive for the placement of the AIB distal neurite in
455 the nerve ring, we ectopically increased *syg-1* levels of expression in the proximal
456 neighborhood. Through promoter screening and lineage-based cell identification, we
457 determined that during embryogenesis, promoters of the *nphp-4* and *mgl-1b* genes are
458 primarily expressed in neurons of the proximal neighborhood
459 (http://promoters.wormguides.org.) (Z. Bao et al., 2006; Boyle et al., 2006; Duncan et

al., 2019). Many of the neurons in which these promoters are expressed are fasciculation partners of AIB in the proximal neighborhood. We used these promoters to drive ectopic expression of a *syg-1* cDNA in the proximal neighborhood in the *syg-1(ky652)* mutant background. Unlike in wild type and *syg-1* mutants (Fig. 7a-f, Supplementary Fig. 9a,b), in the animals with ectopic *syg-1* expression, we observed a gain-of-function phenotype in which the AIB distal neurite remains partially positioned in the proximal neighborhood through postembryonic larval stages (Fig. 7g-j, Supplementary Fig. 9c). Therefore ectopic expression of *syg-1* in neurons of the proximal neighborhood is sufficient to misposition the AIB distal neurite segment. When we ectopically expressed a *syg-1* cDNA lacking the intracellular domains, we observed similar gain-of-function effects, indicating that SYG-1's extracellular Ig domains are sufficient in this context (Supplementary Fig. 9d). These observations suggest that SYG-1 is instructive in the placement of the AIB distal neurite into specific neighborhoods, and that its spatiotemporally regulated expression in banded patterns in the nerve ring is important for placement of specific neurites onto distinct neuropil layers.

SYG-1 is required for layer-specific placement of rich-club neuron AVE

We next examined if *syg-1* is also important for placement of other neurites in the layers in which it is highly expressed. We focused on the rich-club AVE neurons, the neurites of which are also placed in two distinct neighborhoods, different from the AIB neighborhoods and separated by a posterior-anterior chiasm at the dorsal midline. (Fig. 8a-c)(Moyle et al., 2020; Sabrin et al., 2019; Towlson et al., 2013; White et al., 1986).

Reconstructions from electron micrographs reveal that the AVE neurons have a morphology similar to AIB, however its neurite is more anteriorly placed (by one stratum) with respect to AIB (Moyle et al., 2020). Therefore the proximal neurite of AVE occupies the S2/S3 neighborhood occupied by the AIB distal neurite. Since *syg-1* expression is enriched in this "AIB distal/AVE proximal" neighborhood, we tested, by examining AVE neurite placement relative to the RIM neurons, if placement of the AVE neurite in this neighborhood is also affected in *syg-1(ky652)* mutants.

Although AVE and RIM are not synaptic partners, they form non-synaptic contacts with each other along their neurites, as indicated by EM connectome data (White et al., 1986; Witvliet et al., 2020). When we fluorescently labeled RIM and AVE in wildtype animals, we observed that the proximal AVE neurite runs along the RIM neurite, consistent with the EM studies (Fig. 8d,e,e'). By contrast, in *syg-1* mutants the AVE proximal neurite is frequently detached from RIM (seen in 50% of *syg-1(ky652)* mutants versus 9.1% in wild type (Fig. 8f,g,g',h). The dorsal midline shift of AVE is also affected in *syg-1* mutant animals (mean length = 2.73 μm in *syg-1(ky652)* and 3.99 μm in wild type animals; Fig. 8i). Together with the AIB studies, these observations are consistent with *syg-1* expression in a S2/S3 sublayer resulting in nanoscale placement of both the AIB and AVE neurites into that neighborhood.

In the previous sections we demonstrated that RIM has robust *syg-1* expression during nerve ring development and throughout postembryonic stages. So we next investigated if RIM acts as a guidepost, positioning AVE onto the S2/S3 neighborhood to facilitate formation of AVE synapses onto correct partners. We observed that caspase-mediated ablation of the RIM neurons results in partial defects in the

506 placement of the AVE proximal neurite (37.03% of RIM-ablated animals had defects in
507 AVE neurite placement, compared to 6.37% in wild type animals) (Fig. 8j,k). Our
508 observations suggest that layer-specific expression of *syg-1* regulates nanoscale
509 precision in placement of the AVE neurites in the AVE proximal neighborhood.
510 Together, our studies uncover spatiotemporal dynamics of expression of an adhesion
511 molecule between nerve ring neighborhoods, and its regulation of a novel zippering
512 mechanism for positioning neurites onto these specific neuropil strata.
513

514 **Discussion**

515 Nanoscale placement of rich-club interneuron AIB results in the wiring of modular
516 circuits across distinct layers of the neuropil. Neuropil layers are a conserved
517 organizational principle present in evolutionarily diverse brain regions, ranging from the
518 *C. elegans* nerve ring to the *Drosophila* lamina and the inner plexiform layer of the
519 mammalian retina (Moyle et al., 2020; Robles et al., 2011; Tan et al., 2015). Precise
520 placement of neuronal processes and their synapses, particularly for neurons spanning
521 across multiple layers, underpin brain topographic maps, and their functional and
522 structural principles (Clandinin & Feldheim, 2009). We find that in the layered nematode
523 nerve ring, “rich-club” interneuron AIB facilitates network connectivity between the
524 modular S2, S3 and S4 layers, and that its precise placement and synaptic distribution
525 in the context of the neuropil is tightly linked to its functional properties as a rich-club
526 informational hub across layers. The conserved and stereotyped design principles
527 observed for AIB, both by EM analyses and *in vivo*, are reminiscent of those seen for
528 cellular motifs in the inner plexiform layer of the vertebrate retina. For example, AII

amacrine cells, which distribute their neurites and synapses across distinct, but specific sublaminae, receive inputs from rod bipolar axon terminals (in lower sublamina b) and produce outputs onto ganglion cell dendrites (in sublamina a)(Kolb, 1995; Strettoi et al., 1992). Our forward genetic screens in AIB reveal that the developmental processes dictating neurite placement, and those instructing polarized distribution of pre- and postsynaptic specializations across laminae, are genetically separable. Therefore in AIB, the correct emergence of conserved design principles requires the modular deployment of two developmental programs: polarized placement of pre- and postsynaptic specializations along the neurite, and the nanoscale placement of the neurite onto the correct neighborghood of the neuropil.

A novel zippering mechanism governs precise AIB placement onto specific neighborhoods in the neuropil. The correct development of the neuropil structure requires that 181 neurites, which form synapses *en passant* or along the length of their axon, are precisely placed onto neighborhoods within layers. Our current mechanistic frameworks of neurodevelopment are insufficient to explain how single cells make simultaneous and coordinated use of similar molecular cues to achieve precise placement onto specific neighborhoods within the layered neuropil. By combining light sheet microscopy, a new triple-view confocal microscope and machine learning approaches, we are able to resolve these developmental events for the AIB neurons of *C. elegans*, and uncover an *in vivo* mechanism that places neurites onto layers via zippering. Zippering has been observed and characterized in tissue culture cells, and has been hypothesized to be a mechanism that could instruct neurites switching tracts within bundles or fascicles (Honig et al., 1998; Šmít et al., 2017). Evidence for the *in*

552 *vivo* existence of this mechanism, or its importance in development, has been lacking.
553 We now demonstrate that zippering occurs *in vivo* in embryos, and that it is important
554 for placing neurites within specific neuropil neighborhoods during development.

555 Spatiotemporally-regulated expression of IgCAM protein SYG-1 in specific nerve
556 ring neighborhoods guide placement of AIB neurites. Our genetic studies, embryonic
557 expression studies and imaging analyses reveal that expression of this IgCAM in
558 specific nerve ring neighborhoods is dynamic, coincides with AIB developmental
559 decisions, and is necessary, non-autonomously, for AIB neurite placement onto specific
560 layers. Our findings are consistent with studies in the *Drosophila* medulla, which
561 determined that expression of DIP family of IgCAMs are restricted to specific layers or
562 layer boundaries, regulated during pupal development and probably necessary for
563 matching neuronal pairs within medullar layers (Tan et al., 2015). Moreover,
564 spatiotemporal dynamics of adhesion molecule expression encodes layer specificity in
565 the lamina of the *Drosophila* visual system, e.g., it was found that expression of the
566 adhesion molecule Cadherin-N renders neurons competent to layer-specific targeting in
567 a temporally segregated manner (Petrovic & Hummel, 2008). Our observations extend
568 these findings, now demonstrating that the spatiotemporal regulation of SYG-1 in
569 specific *C. elegans* nerve ring neighborhoods is tightly coordinated with the sequential
570 cellular decisions of AIB during the placement of its neurite segments onto specific
571 layers within the neuropil.

572 SYG-1 expression is sufficient to instruct misplacement of AIB onto ectopic
573 neighborhoods. Expression of the *syg-1* gene, first at the S3/S4 nerve ring
574 neighborhood and later at the S2/S3 neighborhood coincides with the AIB outgrowth

575 dynamics through these neighborhoods. Mis-expression of SYG-1 is sufficient to result
576 in the retention of segments of the AIB neurite onto the incorrect layer, indicative of a
577 role for SYG-1 in instructing zippering and placement of AIB onto the proper neuropil
578 layer. The Ig-CAM SYG-1 is conserved across evolution, and its orthologs (Rst and
579 Kirre in *Drosophila* and Kirrel1/2/3 in mammals) play important roles as adhesion
580 molecules in varying developmental contexts (S. Bao & Cagan, 2005; Garg et al., 2007;
581 Kim et al., 2015; Serizawa et al., 2006; Shen & Bargmann, 2003; ztokatli et al., 2012).
582 We note that while in the *C. elegans* egg-laying circuit, SYG-1 is known to interact with
583 its partner (SYG-2) to regulate synapse formation, in the context of the nerve ring, these
584 molecules appear to primarily mediate fasciculation. A loss-of-function mutant allele of
585 *syg-2* exhibits similar defects in AIB distal neurite placement (Supplementary Fig. 4d-f).
586 A loss of function mutant in *syg-2* has been previously shown to result in defasciculation
587 defects of the HSNL axon (Shen et al., 2004), and while not characterized in this study,
588 we hypothesize that similar mechanisms might underpin *syg-2* roles at the nerve ring.
589 Importantly, our findings suggest that SYG-1 role in neurite placement in nerve ring
590 neighborhoods is analogous to the role for mammalian orthologs Kirrel 2 and Kirrel3,
591 which are involved in axon sorting in the olfactory system, possibly via regulation of
592 axon fasciculation.

593 Zippering mechanisms via affinity-mediated adhesion might help instruct
594 neighborhood coherence while preserving 'fluid', or transient interactions among
595 neurites within neuropil structures. Our analyses of contact profiles for individual
596 neurons in the nerve ring neuropil reveal that most interactions between neuropil
597 neurites are brief, resulting in a 'tangled' structure with variable contact profiles across

598 connectomes (Moyle et al., 2020). Yet, neuropils, including the *C. elegans* nerve ring,
599 retain structural design features that underlie functional relationships among neurons,
600 and circuit specificity. How does the system solve this tension of flexibility and
601 stereotypicity? We speculate that dynamic expression of adhesion molecules, such as
602 SYG-1, and zippering mechanisms, might help preserve the tissue organization in the
603 tangled context of neuropils by creating affinity relationships of relative strengths. These
604 relationships could result in the separation of neuropil clusters, similar to observations in
605 developing embryos in which cell types expressing compatible cell adhesion molecules
606 were observed to phase separate onto clusters based on affinity relationships (Foty &
607 Steinberg, 2005, 2013; Steinberg, 1962). Our observations of the expression of SYG-1
608 simultaneously coordinating, not only AIB development, but also laminar placement of
609 rich club neuron AVE, suggest a layer-specific molecular signature that influences co-
610 segregation of neighboring neurites via affinity profiles. We hypothesize that in
611 neuropils, these layer-specific molecular signatures mark specific domains that enable
612 placement of neurites via flexible, differential cell-adhesion mediated zippering
613 mechanisms.
614

615 ## Methods

616

617 ### *C. elegans* strains

618 *C. elegans* strains were raised at 20°C using OP50 *Escherichia coli* seeded on
619 NGM plates. N2 Bristol is the wild-type reference strain used. We received the NC1750

620 strain from the Caenorhabditis Genetics Center (CGC). Transgenic strains used in this
621 study are available upon request.
622
623 **Molecular biology and Transgenic lines**
624 We used Gibson Assembly (New England Biolabs) or the Gateway system
625 (Invitrogen) to make plasmids used for generating transgenic *C. elegans* strains.
626 Detailed cloning information or plasmid maps will be provided upon request. Transgenic
627 strains were generated via microinjection with the construct of interest at 5-100 ng/uL by
628 standard techniques (Mello & Fire, 1995). Co-injection markers *unc-122p*: GFP or *unc-*
629 *122p*: RFP were used.
630 We generated the *syg-1* transcriptional reporter (Fig. 4a-h, Fig.6, Supplementary
631 Fig. 8) by fusing membrane-targeted PH:GFP to a 3.5 kb *syg-1* promoter region as
632 described (Schwarz et al., 2009).
633
634 **SNP mapping and Whole-Genome Sequencing**
635 We isolated mutant allele *daf-16(ola337)* and *syd-2(ola341)* from a visual forward
636 genetic screen in an integrated wild type transgenic strain (*olaIs67*) with AIB labeled
637 with cytoplasmic mCherry and AIB presynaptic sites labeled with GFP: RAB-3. Ethyl
638 methanesulfonate (EMS) mutagenesis was performed and animals were screened for
639 defects in placement of the AIB neurite, and defects in AIB presynaptic site distribution.
640 We screened F2 progeny on a Leica DM 5000 B compound microscope with an HCX
641 PL APO 63x/1.40–0.60 oil objective.

642 The novel lesions *ola337* and *ola341* were out-crossed six times to wild type (N2)
643 animals and still retained a defect in AIB distal neurite placement and AIB presynaptic
644 protein distribution, respectively. We then used single-nucleotide polymorphism (SNP)
645 mapping as described (Davis et al., 2005) to map the *ola337 and ola341* lesions.

646 We then performed whole-genome sequencing on *ola337* and *ola341* (along with
647 4 other mutants from the screen) at the Yale Center for Genome Analysis (YCGA), as
648 previously described (Sarin et al., 2008). We analyzed the results using the Galaxy
649 platform, with http://usegalaxy.org/cloudmap (Minevich et al., 2012) using the EMS
650 variant density mapping workflow. Lesion information from mutants is listed in
651 Supplementary Table 1.
652

653 **Confocal imaging of *C. elegans* larvae and image processing**

654 We used an UltraView VoX spinning disc confocal microscope with a 60x CFI
655 Plan Apo VC, NA 1.4, oil objective on a NikonTi-E stand (PerkinElmer) with a
656 Hammamatsu C9100–50 camera. We imaged the following fluorescently tagged fusion
657 proteins, eGFP, GFP, PH:GFP (membrane-tethered), RFP, mTagBFP1 and mCherry at
658 405, 488 or 561 nm excitation wavelength. We anesthetized *C. elegans* at room
659 temperature in 10mM levamisole (Sigma) under glass coverslips and mounted them on
660 glass slides for imaging.

661 We used the Volocity image acquisition software (Improvision by Perkin Elmer)
662 and processed our images using Fiji(Schindelin et al., 2012). Image processing included
663 maximum intensity projection, 3D projection, rotation, cropping, brightness/contrast, line
664 segment straightening, and pseudo coloring. All quantifications from confocal images

were conducted on maximal projections of the raw data. The simple neurite tracer Fiji plugin and a MATLAB code were used to validate estimation of minimum perpendicular distance between neurites. Pseudocoloring of AIBL and AIBR was performed in Fiji. Pixels corresponding to the neurite of either AIBL/R were identified and the rest of the pixels in the image were cleared. This was done for both neurons of the pair and the resulting images were merged.

Embryo labeling, imaging and image processing

For labeling of neurites and subcellular structures in embryos, we used membrane tethered PH:GFP. A subtractive labeling strategy was employed for AIB embryo labeling (Supplementary Fig. 6a). Briefly, we generated a strain containing unc-42p::ZF1::PH::GFP and lim-4p::SL2::ZIF-1, which degraded GFP in the sublateral neurons, leaving GFP expression only in the AIB and/or ASH neurons. (Armenti et al., 2014b). Onset of twitching was used as a reference to time developmental events. Embryonic twitching is stereotyped and starts at 430 minutes post fertilization (m.p.f) for our imaging conditions.

Embryonic imaging was performed via dual-view inverted light sheet microscopy (diSPIM) (Kumar et al., 2014; Wu et al., 2013) and a combined triple-view line scanning confocal/DL for denoising, as described below.

Triple-view line-scanning confocal/DL

We developed a triple-view microscope that can sequentially capture three specimen views, each acquired using line-scanning confocal microscopy. Multiview

688 registration and deconvolution can be used to fuse the 3 views (Wu et al., 2013),
689 improving spatial resolution. Much of the hardware for this system is similar to the
690 previously published triple-view system (Wu et al., 2016), i.e., we used two 0.8 NA
691 water immersion objectives for the top views and a 1.2 NA water immersion lens placed
692 beneath the coverslip for the bottom view. To increase acquisition speed and reduce
693 photobleaching, we applied a deep-learning framework (Weigert et al., 2018) to predict
694 the triple-view result when only using data acquired from the bottom view. The training
695 datasets were established from 50 embryos (anesthetized with 0.3% sodium azide) in
696 the post-twitching stage, in which the ground truth data were the deconvolved triple view
697 confocal images, and the input data were the raw single view confocal images resulting
698 in improved resolution (270nm X 250 nm X 335nm).
699

700 **Cell lineaging**

701 Cell lineaging was performed using StarryNite/AceTree (Z. Bao et al., 2006;
702 Boyle et al., 2006; Murray et al., 2006). Light sheet microscopy and lineaging were
703 integrated to uncover cell identities in pre-twitching embryos (Duncan et al., 2019).
704 Lineaging information for promoters is available at http://promoters.wormguides.org.
705 Our integrated imaging and lineaging approaches enabled us to identify a promoter
706 region of *inx-19* which is expressed in the RIM neurons prior to RIM neurite outgrowth
707 (~370 m.p.f.) and in additional neurons in later embryonic stages. The *inx-19p* was one
708 of the promoters used for embryonic ablation of RIM (described in the next section).
709 In addition our integrated imaging and lineaging approach also enabled us to identify
710 two promoters with expression primarily in the AIB proximal neighborhoods (*nphp-4*p

and *mgl-1b*p). 4/4 neuron classes that were identified to have *nphp4*p expression, are in the AIB proximal neighborhood (ADL/R,ASGL/R,ASHL/R,ASJL/R) and 2/3 neuron classes that were identified to have *mgl-1b*p expression are in the AIB proximal neighborhood (AIAL/R, ADFR) (http://promoters.wormguides.org).

Caspase-mediated ablation of RIM neurons

The RIM neurons were ablated using a split-caspase ablation system (Chelur & Chalfie, 2007). We generated one set of transgenic strains with co-expression of the p12 or p17 subunit of human Caspase-3, both expressed under *inx-19p* (termed ablation strategy 1), and another set of ablation strains with co-expression of the p12 subunit expressed under *inx-19p* and p17 under *tdc-1p* (termed ablation strategy 2) (Supplementary Fig. 5). L3 larvae from the RIM-ablated populations were imaged on the spinning-disk confocal microscope (described earlier).

Rendering of neurites and contacts in the EM datasets

From available EM datasets (C. Brittin et al., 2018; Cook et al., 2019; White et al., 1986; Witvliet et al., 2020) we rendered the segmentations of neuron boundaries in 2D using TrakEM2 in Fiji. TrakEM2 segmentations were volumetrically rendered by using the 3D viewer plugin in Fiji (ImageJ2; downloaded from https://imagej.net/Fiji#Downloads) and saved as object files (.obj), or by using the 3d viewer in CytoSHOW (Duncan et al., 2019), an open source image analysis software. CytoSHOW can be downloaded from http://www.cytoshow.org/ as described.

733 To generate 3D mappings of inter-neurite membrane contact, the entire
734 collection of 76,046 segmented neuron membrane boundaries from the JSH TEM
735 datasets (C. Brittin et al., 2018; C. A. Brittin et al., 2020; White et al., 1986) were
736 imported from TrakEM2 format into CytoSHOW as 2D cell-name-labelled and uniquely
737 color-coded regions of interest (ROIs). To test for membrane juxtaposition, we dilated
738 each individual cell-specific ROI by 9 pixels (40.5 nm) and tested for overlap
739 with neighboring undilated ROIs from the same EM slice. A collection of 289,012
740 regions of test-overlap were recorded as new ROIs, each bearing the color code of the
741 dilated test ROI and labeled with both cell-names from the pair of test-overlapped
742 ROIs. These "contact patch" ROIs were then grouped by cell-pair-name and rendered
743 via a marching cubes algorithm to yield 3D isosurfaces saved in .obj files. Each of the
744 8852 rendered .obj files represents all patches of close adjacency between a given pair
745 of neurons, color-coded and labeled by cell-pair name. Selected .obj files were co-
746 displayed in a CytoSHOW3D viewer window to produce views presented in Figures.
747

748 **Cosine similarity analysis for comparing AIB contacts across connectomes**

749 We performed cosine similarity analysis (Han et al., 2012) on AIB contacts in
750 available connectome datasets (C. Brittin et al., 2018; Cook et al., 2019; Witvliet et al.,
751 2020). For each available adjacency dataset(C. Brittin et al., 2018; Moyle et al., 2020;
752 Witvliet et al., 2020), we extracted vectors comprising of number of AIB contacts with
753 neurons common to all the datasets. We then performed cosine similarity analysis on
754 these vectors using the formula:

$$\frac{\sum_{i=1}^{n} A_i B_i}{\sqrt{\sum_{i=1}^{n} A_i^2}\sqrt{\sum_{i=1}^{n} B_i^2}}$$

where A and B are the two vectors under consideration with the symbol “i” denoting the i-th entry of each vector. The similarity values were plotted as a heat map for AIBL and AIBR using Prism. For the datasets L1_0hr, L1_5hr, L1_8hr, L2_23hr, L3_27hr, L4_JSH and Adult_N2U, the neuron-neuron contacts in the EM sections corresponding to the nerve ring were used.

Betweenness centrality analysis

We analyzed betweenness centrality for two of the available connectomes of different developmental stages (L1 and adult) (Witvliet et al., 2020). By treating individual components (mostly neurons) of a connectome as the vertices of a graph, we use the following definition of Betweenness Centrality for a vertex v,

$$BC(v) = \sum_{s,t:s\neq t\neq v} \frac{\lambda_{st}(v)}{\lambda_{st}}.$$

Here $\lambda_{st}(v)$ denotes the number of shortest paths between the vertices s and t, that include vertex v, whereas λ_{st} denotes the total number of shortest paths between the vertices s and t. We finally divide $BC(v)$ by $(N-1)(N-2)/2$ to normalize it to lie between 0 and 1. For our implementation we use the Brain Connectivity Toolbox (Rubinov & Sporns, 2010) of MATLAB2020, in particular, the function “betweenness_bin.m” in which we input the binary connection matrix corresponding to the L1 and adult connectomes (Witvliet et al., 2020). We made a Prism box plot (10 to

775 90 percentile) of betweenness centrality values of all components in each of the two
776 connectomes and highlighted the betweenness centrality values for AIBL and AIBR.

777

778 **Image representation, quantification and statistical analysis**

779 **Representation of AIB and AVE from confocal images –** Since we observed that the
780 proximal and distal neurites of AIBL and AIBR completely align and overlap
781 (Supplementary Fig. 1k-m) in confocal image stacks where the worms are oriented on
782 their side, for representation purposes we have used the upper 50% of z-slices in
783 confocal image stacks to make maximum intensity projections. This shows the proximal
784 neurite of AIBL in the context of the distal of AIBR (which has the same anterior-
785 posterior position as the distal neurite of AIBL) (Supplementary Fig. 2k-m), or vice
786 versa. We used the same procedure for AVEL and AVER.

787 **Quantification of penetrance of mutant phenotypes –** The percentage of mutant or
788 ablation animals exhibiting a normal AIB distal neurite trajectory was determined by
789 visualizing and scoring under the Leica compound microscope described. Animals in
790 which distal neurites of both AIBL or AIBR were placed at a uniform distance from the
791 proximal neurites were scored as having normal AIB distal neurite trajectory. The same
792 scoring protocol was followed for determining percentage of animals having normal AVE
793 distal neurite trajectory.

794 **Quantification of minimum perpendicular distance between neurites –** Minimum
795 perpendicular distances between neurites were measured by manually creating a
796 straight line selection (on Fiji) between the neurites (perpendicular to one of the

neurites) in the region where the gap between them is estimated to be the smallest. The measurements were done on maximum intensity projections of raw confocal image stacks where the worms are oriented on their side (z-stacks acquired along left right axis of the worm, producing a lateral view of the neurons).

Quantification of percent detachment between neurites – The percent detachment for defasciculated neurites (AIB and RIM or AVE and RIM) is calculated by the formula % detachment = detached length (L_d) x 100 /total length (L_t) (also shown in Fig. 3m). L_d is calculated by making a freehand line selection along the detached region of the RIM neurite and measuring its length and L_t is calculated by making a freehand selection along the RIM neurite for the entire length over which it contacts AIB or AVE, and measuring the length of the selection. All the measurements were performed on maximum intensity projections of confocal image stacks where the worms are oriented on their side (z-stacks acquired along left right axis of the worm, producing a lateral view of the neurons).

Quantification of relative (distal) enrichment of *syg-1* reporter expression in neighborhoods – Relative (distal) enrichment of *syg-1* reporter expression is calculated using the formula (also shown in Fig. 4i), Relative enrichment (*syg-1p*) = mean distal neighborhood intensity (I_d)/mean proximal neighborhood intensity (I_p). These measurements were done in transgenic animals co-expressing the AIB reporter and the *syg-1* transcriptional reporter. For calculation of I_p a freehand line selection was made (using Fiji) along the band of *syg-1* expression along the AIB proximal neurite (as visualized with the AIB marker) and mean intensity along the selection is calculated. Same was done for calculation of I_d except along the AIB distal neurite. The ratios of I_d

and I_p were plotted as relative (distal) enrichment values. These values were calculated from maximum intensity projections of confocal image stacks where the worms are oriented on their side (z-stacks acquired along left right axis of the worm, producing a lateral view of the neurons). I_d/I_p was calculated from the side of the animal closer to the objective, consistently across images to avoid differences due to depth artifacts.

Quantification of the dorsal midline shift (chiasm) length of AIB and AVE – The dorsal midline shift (chiasm) lengths of AIB and AVE were calculated by making 3D maximum intensity projections of confocal z-stacks and orienting the neuron pair to a dorsal-ventral view. A straight line selection is made along the posterior-anterior shift of each neuron and its length measured using Fiji.

Quantification of distal neurite length of AIB – The length of the distal neurite of AIB was measured by drawing a freehand line along the region of the neurite past the proximal neurite in maximum intensity projections of confocal image stacks where the worms are oriented on their side (z-stacks acquired along left right axis of the worm, producing a lateral view of the neurons).

Quantification of the relative position of the AIB neurite during embryogenesis – The distances of the unzippering and zippering forks from the dorsal midline in Fig. 5l and 5m are calculated from deconvolved maximum intensity projections of diSPIM images where the neurons are oriented in an axial view. These distances are lengths along the AIB neurite from the unzippering/zippering forks to the dorsal midline.

The distance of the zippering fork from the midline is subtracted from the total length of the neurite at each timepoint to obtain the length of overlap between AIB and

RIM. The fraction of the length of AIB-RIM overlap to the total AIB neurite length multipled by 100, yields a percentage overlap value at every timepoint. The reported values of percent overlap are averages across the three independent embryo datasets used for the Fig. 5m plot. These measurements are performed with CytoSHOW. We performed the same steps as with the confocal images to pseudocolor the neurites for representation.

Quantification of the angle of exit of the developing AIB distal neurite and ventral turn of nerve ring in embryos – The angle of exit of the developing AIB distal neurite is measured as the angle between straight line tangents drawn along the separating distal segment of AIBL and the proximal neurite of AIBR and vice versa. These measurements are performed on deconvolved maximum intensity projections of diSPIM images where the neurons are oriented in an axial view. The angle of ventral turn of the nerve ring is measured as the angle between straight line tangents drawn along segments of the nerve ring on either side of the ventral bend of the nerve ring (see Supplementary Fig. 6h,i). These measurements are performed with CytoSHOW.

Imaging and representation of synaptic protein RAB-3 in AIB in embryos – Time-lapse imaging of presynaptic protein RAB-3 in AIB in embryos was performed using diSPIM. To visualize the distribution of RAB-3 along the neurite we straightened the distal neurite of each AIB neuron from maximum intensity projections where the AIB neurons are oriented in the axial view.

Statistical analyses

Statistical analyses were conducted with PRISM 7 software. For each case, the chosen statistical test is described in the figure legend and "n" values are reported. Briefly, for continuous data, comparisons between two groups were determined by the Student's t test. Error bars were reported as standard errors of the mean (SEM). For categorical data, groups were compared with Fisher's exact test. The p values for significant differences are reported in the figure legend.

Acknowledgements

We thank Kang Shen, Harald Hutter and John Murray for providing strains and constructs. We thank Scott Emmons, Steve Cook, and Chris Brittin, and Mei Zhen and Daniel Witvliet for sharing their segmented EM data and adjacencies. We thank members of the Colón-Ramos lab for help, advice and insightful comments during manuscript preparation. We thank the Caenorhabditis Genetics Center (funded by NIH Office of Research Infrastructure Programs P40 OD010440) for *C. elegans* strains. We thank the Research Center for Minority Institutions program, the Marine Biological Laboratories (MBL), and the Instituto de Neurobiología de la Universidad de Puerto Rico for providing meeting and brainstorming platforms. H.S. and D.A.C-R. acknowledge the Whitman and Fellows program at MBL for providing funding and space for discussions valuable to this work. Research in the D.A.C-R., W.A.M., and Z. B. labs were supported by NIH grant No. R24-OD016474. Research in H.S. lab was further supported by the intramural research program of the National Institute of Biomedical Imaging and Bioengineering (NIBIB), NIH.

887 Research in Z.B. lab was further supported by an NIH center grant to MSKCC
888 (P30CA008748). Research in the D.A.C.-R. lab was further supported by NIH
889 R01NS076558, DP1NS111778 and by an HHMI Scholar Award.

890

891

892 ## Figure Legends

893

894 **Figure 1. Design principles of AIB neurite placement and synaptic positions**
895 **enable it to link two neighborhoods in the nerve ring**

896

897 **(a)** Schematic of an adult/larval *C. elegans* showing an AIB neuron (cyan) and its
898 proximal (orange) and distal (magenta) neighborhoods. The AIB neurite has a proximal
899 neurite segment (orange arrow), a posterior-anterior shift (black arrowhead, herein also
900 referred to as chiasm) at the dorsal midline (dashed straight line) and a distal neurite
901 segment (magenta arrow; on the other side of the worm, AIB cyan color muted in the
902 distal segment to reflect the position behind the pharynx, which is in gray). The region
903 occupied by the nerve ring neuropil is depicted in light brown. Note that this schematic
904 only shows one neuron of the AIB pair (AIBR and AIBL, for right and left, respectively,
905 see Supplementary Fig. 1e-j for both AIBs). Cell body is marked with an asterisk.
906 **(b,c)** Volumetric reconstruction of AIBR from the JSH electron microscopy connectome
907 dataset (White et al., 1986) in lateral (b) and axial (c) views. Postsynaptic (red) and
908 presynaptic (yellow) regions of the neurite, based on connectivity maps of AIBR, are
909 indicated. Note that the postsynaptic and presynaptic regions coincide with the proximal

and distal segment of the neurites, in (a). Arrowhead points to the chiasm (formed by the posterior-anterior shift at the dorsal midline). Scale bar = 1 μm

(d,e) Representative confocal image showing lateral (d) and axial (e) view of an AIB neuron with postsynaptic sites (red, labeled by GLR-1:GFP) and presynaptic sites (yellow, labeled by mCh:RAB-3). Cell-specific expression of GLR-1 and RAB-3 was achieved by using a bashed *inx-1* promoter (http://promoters.wormguides.org) (Altun et al., 2008). Arrowhead points to the chiasm. Cell body is marked with an asterisk. Scale bar = 10 μm, also applies to (e).

(f,g) Schematic of AIB (corresponding to the dashed box region in (a) and also images in (b-e)), showing lateral (f) and axial (g) views of an AIB neuron (cyan) in the context of the proximal (orange) and distal (magenta) neighborhoods in the nerve ring (light brown). Dashed line represents the dorsal midline.

(**h,i**) Representative confocal image from a wild type L4 animal showing an AIB neuron labeled with cytoplasmic mCherry (cyan) in lateral (h) and axial (i) views. Scale bar = 10 μm, also applies to (i-m).

(j,k) Representative confocal image from a wild type L4 animal showing an AIB interneuron labeled with cytoplasmic mCherry (cyan); and RIM motor neuron labeled with cytoplasmic GFP (magenta) in lateral (j) and axial (k) views. RIM-specific labeling was achieved by a *cex-1* promoter (Piggott et al., 2011) (http://promoters.wormguides.org). Note the colocalization of the AIB distal neurite with the distal neighborhood marker RIM. The orange and magenta arrows indicate the positions of the proximal and distal neighborhoods along the anterior-posterior axis. Arrowhead indicates the chiasm.

933 **(l-m)** As (j,k), but with AIB (cyan) and AWC and ASE sensory neurons (orange). AWC
934 and ASE labeling was achieved by a *ceh-36* promoter (Lanjuin et al., 2003; Walton et
935 al., 2015) (http://promoters.wormguides.org). Note the colocalization of the AIB proximal
936 neurite with the proximal neighborhood markers AWC and ASE.
937
938 **Figure 2. Polarized distribution of synaptic proteins in the AIB neurite, and AIB**
939 **neurite neighborhood placement in the neuropil, are genetically separable**
940
941 **(a-d)** Representative confocal image (a-c) and schematic (d) of AIB expressing
942 cytoplasmic mCherry (a) and GFP:RAB-3 (b) in wild type L4 animals for simultaneous
943 visualization of neurite morphology and distribution of presynaptic sites. Merged image
944 (c). Cell body is marked with an asterisk. Scale bar = 10 μm, applies to panels (a-k).
945 **(e-l)** As (a-d) but in the genetic background of a novel *daf-16* mutant allele, *ola337* ((e-h;
946 see also Supplementary Table 1) and in *unc-33(e204)* mutants (i-l). Note GFP:RAB-3
947 polarized distribution to the distal parts of the neurite even in animals displaying severe
948 axon truncation, or displaying morphology and placement defects of the AIB neurite in
949 the context of the neuropil neighborhoods (also see Supplementary Fig. 3).
950
951 **Figure 3. SYG-1 is required for precise placement of the AIB distal neurite to the**
952 **distal, RIM-containing neighborhood**
953
954 **(a-d)** Representative confocal images of AIB (a) and RIM (b) neurons in a wild type
955 animal (L4 stage), and the merged image (c). The dashed box represents the region of

contact between the AIB and RIM neurites, magnified in (d). RIM is the main postsynaptic partner for AIB (White et al., 1986) and co-localizes extensively with AIB distal neurite (Arrow in (d) and Supplementary Fig. 1b,c). Scale bar = 10 μm in (a) applies to (e-g) and (i-k). Scale bar = 1 μm in (d) applies to (h) and (l). Cell bodies are marked with an asterisk.

(e-h) As (a-d) but in the *syg-1(ky652)* mutant background. Note the gap between the AIB distal neurite and the RIM neurites (h), indicating loss of contact between the AIB and RIM neurites due to defective placement of the AIB distal neurite in the RIM (distal) neighborhood.

(i-l) As (a-d) and (e-h) but for a *syg-1(ky652)* mutant animal expressing a rescuing cosmid (C54A10) containing the genomic region of wild type *syg-1.*

(m) Schematic and scatter plot of quantifications of the loss of contacts between the AIB and RIM neurites. The extent of detachment of the AIB distal neurites from RIM, and hence its deviation from the RIM neighborhood, was quantified using the indicated formula (see also Methods). The cyan and magenta neurites in the schematic represent the AIB distal neurite and the RIM neurites, respectively, as in the images. Scatter plot depicts % detachment values for wild type (n=41), *syg-1(ky652)* mutant (n=39) and cosmid rescue animals (n=16). Error bars indicate standard error of the mean (S.E.M.). ****p<0.0001 by unpaired Student's t-test between WT and *syg-1(ky652)*, and between *syg-1(ky652),* and *syg-1(ky652)* rescued with *syg-1* containing cosmid (C54A10) (called *syg-1* rescue in graph).

(n) Schematic and scatter plot of quantification of minimum perpendicular distance between the AIB proximal and distal neurites. Schematic indicates AIB (cyan) and RIM

(magenta) neurons in the context of the nerve ring (light brown) in WT and *syg-1(ky652)*. Double-headed arrows indicate perpendicular distance between the AIB proximal and distal neurites in WT and *syg-1(ky652)*, respectively. Scatter plot depicts minimum perpendicular distance values for wild type (n=19), *syg-1(ky652)* mutant (n=29) and cosmid rescue animals (n=12) (see Methods). Error bars indicate standard error of the mean (S.E.M.). ****p<0.0001 by unpaired Student's t-test between WT and *syg-1(ky652)*, and between *syg-1(ky652)* and *syg-1(ky652)* rescued with *syg-1* containing cosmid (C54A10) (called *syg-1* rescue in graph).

Figure 4. The SYG-1-expressing RIM neurons regulate AIB distal neurite position

(a-d) Representative confocal image of a wild type L3 animal co-expressing (a) a membrane-targeted *syg-1* transcriptional reporter (see Methods) and (b) cytoplasmic mCherry driven by the AIB-specific promoter (*inx-1p)*. (c) is a merge image of (a) and (b). Since the *syg-1* reporter is membrane-targeted, it labels cell body outlines and neurites (a,c). The dashed box or inset in (c) represents the region of contact between AIB and neurites expressing the *syg-1* reporter, magnified in (d). Note that the *syg-1* reporter shows two bands of expression in the nerve ring (a and c) which coincide with the proximal and distal AIB neurites (b) and neighborhoods (orange and magenta arrows). Note also that there is no membrane outline corresponding to the AIB cell body (a, we drew a dashed siluette of the AIB cell body position as determined in (b)), consistent with the *syg-1* reporter not being expressed in AIB. Asterisk indicates cell

body. Scale bar in (a) = 10 μm, also applies to (b-c) and (e-g). Scale bar in (d) = 1 μm, also applies to (h).

(e-h) As (a-d), but with mTagBFP1 driven by RIM-specific promoter, *cex-1p*. Note the RIM neurite colocalizes with the anterior band of *syg-1* expression, coincident with the AIB distal neighborhood (magenta arrow). The white arrowhead in (e-g) and semi-transparent magenta outline in (e) indicates colocalization of the RIM cell body with the *syg-1* reporter.

(i) Schematic (left) and scatter plot quantification (right) of the expression pattern of the *syg-1* reporter at the two AIB neighborhoods. The mean intensities of the *syg-1* reporter in the two neighborhoods were calculated, and the ratios of the mean distal neighborhood intensity (I_d) to the mean proximal neighborhood intensity (I_p) were plotted as the 'Relative enrichment', as shown in schematic and explained in Methods.

(j-o) Confocal images showing AIB (labeled with cytoplasmic mCherry; (j,m)) and RIM (labeled with PH:GFP; (k,n)) and merged images (l,o) for wild type animals (j-l) and animals in which RIM was genetically ablated (m-o). RIM ablation was achieved using Strategy 2, explained in Supplementary Fig. 5 and below. Scale bar = 10 μm, also applies to (k-o).

(p) Quantification of the penetrance of the AIB neurite placement defect as the percentage of animals with normal AIB distal neurite trajectory. Strategy 1 and Strategy 2 refer to split caspase ablations (Chelur & Chalfie, 2007) using two different combinations of promoters expressed in RIM. In Strategy 1, expression of both caspase fragments was driven by an *inx-19* gene promoter. In Strategy 2, expression of one caspase fragment was driven by *inx-19p* and the other fragment by a *tdc-1* gene

promoter ((Alkema et al., 2005); Supplementary Fig. 5 and http://promoters.wormguides.org)). *tdc-1p* drives expression of caspases in RIM later in embryonic development as compared to *inx-19p* (data not shown), resulting in later ablations of RIM, and weaker phenotype. ****p<0.0001 by Fisher's exact test between WT and RIM-ablated populations.

(q) Quantification of the expressivity of the AIB neurite placement defect by measuring the minimum perpendicular distances between the AIB proximal and distal neurites (see Fig. 3n) in WT (n=28) and RIM-ablated populations (n=10 for strategy 1 and n=14 for strategy 2).****p<0.0001 by unpaired Student's t-test between WT and each of the RIM-ablated populations. Error bars indicate standard error of the mean (S.E.M.).

Figure 5. The AIB neurite repositions onto the distal neighborhood via a zippering mechanism

(a) Schematic of axial view of the AIB neuron pair - AIBL (cyan) and AIBR (yellow) in the context of the nerve ring (light brown) and the pharynx (grey), with distal and proximal neighborhood labeled (see Fig. 1).

(b-f) Time-lapse showing initial placement of AIBL and AIBR in the proximal neighborhood and their subsequent separation from this neighborhood. Images are deconvolved diSPIM maximum intensity projections obtained from developing embryos. Neurons were individually pseudocolored to distinguish them (see Methods). The dashed boxes represent the dorsal half of the nerve ring and are magnified in **(b'-f')**. **(b''-f'')** are schematic diagrams representing the images in (b-f). Dashed vertical lines

represent the dorsal midline. Note in (b,b',b''), the AIBL and AIBR neurites approaching the dorsal midline in the proximal neighborhood, see schematic in (a). In (c,c',c''), AIBL and AIBR have met at the dorsal midline and continue growing along each other, past the midline. The latter part of the neurite, past the midline, becomes the future distal neurite. (d,d',d'') shows the tip of the AIBL future distal neurite moving away from the proximal neighborhood and its counterpart, AIBR. The arrowhead indicates the point of separation of the AIBL distal neurite and the AIBR proximal neurite. (e,e',e'') shows further separation of the two neurites and by (f,f',f"), they have completely separated. The arrowheads in (e,e'e'') and (f,f'f'') also indicate the junction between the separating AIBL distal neurite and the AIBR proximal neurite. Scale bar = 10 μm for (b-f) and 2 μm for (b'-f'). All times are in m.p.f. (minutes post fertilization). A similar sequence of events is visualized at higher spatial resolution in Supplementary Fig. 6 using triple-view line scanning confocal microscopy.

(g) Schematic of one AIB neuron (cyan) in the context of distal neighborhood marker RIM (magenta), the nerve ring (light brown) and the pharynx (grey).

(h-j) Time-lapse showing placement of the AIB neurite (cyan) relative to the distal neighborhood marked by RIM (magenta). As in (b-f), images are deconvolved diSPIM maximum intensity projections and the neurons were pseudocolored. The dashed boxes represent the dorsal half of the nerve ring and are magnified in (h'-j'). Dashed line indicates dorsal midline (where the dorsal shift, or chiasm, in the adult is positioned, see Fig. 1). (h''-j'') are schematic diagrams representing the images in (h-j). Note in (h,h',h"), the tip of the AIB neurite encounters the growing RIM neurite (green arrowhead in (h'); black arrowhead in (h"). In (i,i',i''), the AIB distal neurite has partially

aligned along the RIM neurites. The green arrowhead now indicates point of initial encounter of the two neurites (same as in (h') and the white arrowhead (in i') indicates the zippering event bringing the AIB and RIM neurons together in the distal neighborhood (as black arrowhead in i"). In (j,j',j") the two neurites have zippered up to the dorsal midline as indicated by the white arrowhead (j') and black arrowhead (j"). Arrow in (i') indicates direction of zippering. Scale bar = 10 μm for (h-j) and 2 μm for (h'-j'). All times are in m.p.f. (minutes post fertilization).

(k) Confocal micrograph of a postembryonic L4 animal in axial view showing the relationship of AIB-RIM as in (j). The same image as Fig. 1(k) was used as it allows visualization of one AIB of the pair due to mosaic array expression. Scale bar = 10 μm. The region in the dashed box represents dorsal part of the nerve ring, magnified in (k'). Scale bar in (k') = 2 μm.

(l,m) The white arrowheads in d' and i', which correspond to the points at which the neurites are separating or joining, are defined as the unzippering fork and zippering fork respectively. The distances of these points, from the dorsal midline, are quantified in (l) and (m) for different developmental stages in synchronized embryos as indicated in the timepoints on the x-axis (±5 mins). Error bars represent standard error of the mean (S.E.M.), n=5 in (l) and n=3 in (m).

(n) Schematic highlights the three steps by which the AIB distal neurite is repositioned to a new neighborhood – (i) encounter with the new neighborhood; (ii) partial zippering and (iii) complete zippering onto the distal neighborhood (marked by RIM). The term "unzippering" is used to refer to the concomitant AIB detachment from the proximal neighborhood as it is placed to the distal neighborhood via zippering.

Figure 6. Spatiotemporal regulation of *syg-1* expression during embryogenesis correlates with AIB placement in the distal neighborhood

(a) Schematic of the axial view of the AIB neurons (cyan) with the proximal (orange arrows and dashed line) and distal (magenta arrow and dashed line) neighborhoods.
(b-d) Deconvolved diSPIM image of a late stage embryo (~1 hr prior to hatching, or 780 m.p.f.) showing colocalization of the *syg-1* reporter with the AIB proximal and distal neurites (and neighborhoods). This expression pattern of *syg-1* at this late embryonic stage is similar to that observed in postembryonic larvae (Fig. 4a-h). Scale bar = 10 μm, applies in (b-d).
(e-h) Time-lapse images of *syg-1* reporter expression in earlier embryonic stages (450-630 m.p.f.). Images are deconvolved diSPIM maximum intensity projections. The dashed boxes represent the dorsal half of the nerve ring and are magnified in **(i-l)**. **(i'-l')** are schematic diagrams representing the images in (i-l). In (e,i,i') *syg-1* expression is primarily visible in a single band containing amphid neurites, and therefore coincident with the AIB proximal neighborhood. The magenta dashed line and magenta arrows point to the distal neighborhood and the orange arrow, to the proximal neighborhood. (f,j,j') show onset of weak *syg-1* expression in a second neuropil band (white arrow in (j)) and ingrowth of *syg-1*-expressing RIM neurites along this band (white arrowhead, see also Supplementary Fig. 8) onto the distal neighborhood. *syg-1* expression increases in the distal neighborhood and decreases in the proximal neighborhood as embryonic development progresses, and coincident with AIB developmental events that

enable its transition from the proximal to the distal neighborhood (j-l), (Fig. 5a-j). Scale bar = 10 μm in (e-h) and 1 μm in (i-l).

Figure 7. Ectopic *syg-1* expression is sufficient to redirect placement of the AIB distal neurite to ectopic neighborhoods

(a) Schematic of lateral view of a wild type AIB neuron (cyan) in the context of the proximal (orange) and distal (magenta) neighborhoods, and the nerve ring (light brown). SYG-1 endogenous expression higher in the distal neighborhood represented by yellow arrowhead.

(b-c) Confocal image of a wild type L4 animal with AIB (labeled with cytoplasmic mCherry and pseudocolored in cyan) and the proximal neighborhood neurons AWC and ASE (labeled with cytoplasmic GFP and pseudocolored in orange). The dashed box represents the region of contact between AIB and the proximal neighborhood neurons, magnified in (c). Scale bar = 10 μm in (b) (also applies to (e) and (h)) and 1 μm in (c), (also applied to (f) and (i). Cell body is marked with an asterisk.

(d-f) As (a-c) but in the *syg-1(ky652)* lof (loss of function) mutant background. Note that the distal neurite is positioned away from the proximal neighborhood, as in wild type, although these animals display deffects in fasciculation with the distal neighborhood (see Fig. 3).

(g-i) As (a-c) and (d-f) but with ectopic overexpression of *syg-1* cDNA in the proximal neighborhood neurons and in the *syg-1(ky652)* mutant background. In the schematic (g), expression of SYG-1 in the proximal neighborhood (achieved using *nphp-4p*, also

see Supplementary Fig. 9c,d) is represented by yellow arrowhead. Note that the AIB distal neurite is now partially positioned in the proximal neighborhood in which *syg-1* cDNA was ectopically expressed (h,i).

(j) Schematic (left) and scatter plot quantification (right) of minimum perpendicular distances (d_{min}, indicated by black double-headed arrow) between the AIB distal neurite and proximal neighborhood neurons in WT (n=11), *syg-1(ky652)* (n=12), and two *syg-1(ky652)* populations with WT *syg-1* cDNA overexpressed in two different sets of proximal neighborhood neurons via the use of *nphp-4p* and *mgl-1bp* (n=12 and 10 respectively). The *nphp-4p* and *mgl-1bp* promoters are expressed primarily in proximal neighborhood neurons during embryogenesis (http://promoters.wormguides.org). **p<0.01 by unpaired Student's t-test between *syg-1(ky652)* and animals with ectopic proximal WT *syg-1* expression. Error bars indicate standard error of the mean (S.E.M.).

Figure 8. SYG-1 dictates layer-specific placement of rich club interneuron AVE

(a,b) Schematic of the lateral and axial views of command interneuron AVE (green) in the context of its neighborhoods: proximal (magenta) and distal (yellow), with the nerve ring (light brown) and pharynx (grey). Black arrowhead in (a) indicate a posterior-anterior chiasm. The magenta and yellow arrows indicate the positions of the AVE proximal and AVE distal neighborhoods, respectively. Note that while the design principles of AVE are similar to those of rich-club interneuron AIB, their positions in the nerve ring, and the strata they connect, are different (see (c), compare to Supplementary Fig. 1a for AIB).

(c) Volumetric reconstruction of the AVE neuron (green) in the context of the nerve ring strata S2 (purple) and S3 (orange). Note the placement of the AVE proximal neurite along the border of S2 and S3, and the AVE distal neurite at the anterior boundary of S2 (the anterior boundary abuts S1, not shown here). The dashed lines indicate the layer borders. Scale bar = 1 μm.

(d) Confocal image of an L4 animal with AVE and RIM co-labeled. The magenta and yellow arrows indicate the positions of the AVE proximal and AVE distal neighborhoods, respectively. White arrowhead indicates AVE chiasm, corresponding to its anterior shift. Dashed box shows region of contact of the AVE and RIM neurites, magnified in **(e). (e')** is a schematic of the image in (e). Note the region of contact between the AVE proximal neurite and the RIM neurites (e,e'), in the context of AVE, in the AVE proximal neighborhood (as compared to RIM position in AIB distal neighborhood). Scale bar corresponds to 10 μm in (d) and 1 μm in (e). Scale bars in (d) and (e) apply to (f) and (g) respectively. Cell bodies are marked with an asterisk.

(f,g,g') As (d,e,e') but in *syg-1(ky652)* mutant background. Note the gap between the AVE proximal neurite and the RIM neurites (f,g,g') and defect in the dorsal midline shift.

(h) Scatter plot showing quantification of the loss of contacts between the AVE and RIM neurites. The extent of detachment of the AVE proximal neurites from RIM, and hence its deviation from the RIM neighborhood, was quantified using the indicated formula in Fig. 3m (also see Methods). Scatter plot depicts % detachment values for wild type (n=22) and *syg-1(ky652)* (n=16). Error bars indicate standard error of the mean (S.E.M.). **p<0.01 by unpaired Student's t-test between WT and *syg-1(ky652)*.

(i) Quantification of length of the posterior-anterior shift, quantified for each AVE neurite, for WT(n=32) and *syg-1(ky652)* mutants (n=40) and displayed as a scatter plot. Error bars indicate standard error of the mean (S.E.M.). ***p<0.001 by unpaired Student's t-test between WT and *syg-1(ky652)*.

(j) Confocal image of an AVE neuron in L3 animals with RIM neurons ablated using ablation strategy 2 (Supplementary Fig. 5 and Methods). Note altered placement of the AVE proximal neurite with respect to the proximal neighborhood (indicated by the magenta dashed line and the magenta arrow). Scale bar = 10 μm.

(k) The percentage of animals having altered AVE distal neurite trajectory are plotted for WT (n=31) and RIM ablated populations (n=27). *p<0.1 by Fisher's exact test between WT and the RIM-ablated population.

References

Alkema, M. J., Hunter-Ensor, M., Ringstad, N., & Horvitz, H. R. (2005). Tyramine functions independently of octopamine in the Caenorhabditis elegans nervous system. *Neuron*. https://doi.org/10.1016/j.neuron.2005.02.024

Altun, Z. F., Chen, B., Wang, Z. W., & Hall, D. H. (2008). High resolution map of Caenorhabditis elegans gap junction proteins. *Developmental Dynamics*. https://doi.org/10.1002/dvdy.22025

Armenti, S. T., Lohmer, L. L., Sherwood, D. R., & Nance, J. (2014a). Repurposing an endogenous degradation system for rapid and targeted depletion of C. elegans proteins. *Development (Cambridge)*. https://doi.org/10.1242/dev.115048

Armenti, S. T., Lohmer, L. L., Sherwood, D. R., & Nance, J. (2014b). Repurposing an endogenous degradation system for rapid and targeted depletion of C. elegans proteins. *Development (Cambridge)*. https://doi.org/10.1242/dev.115048

Bao, S., & Cagan, R. (2005). Preferential Adhesion Mediated by Hibris and Roughest Regulates Morphogenesis and Patterning in the Drosophila Eye. *Developmental Cell*, *8*(6), 925–935. https://doi.org/https://doi.org/10.1016/j.devcel.2005.03.011

Bao, Z., Murray, J. I., Boyle, T., Ooi, S. L., Sandel, M. J., & Waterston, R. H. (2006). Automated cell lineage tracing in Caenorhabditis elegans. *Proceedings of the National Academy of Sciences of the United States of America*. https://doi.org/10.1073/pnas.0511111103

Barry, J., Gu, Y., & Gu, C. (2010). Polarized targeting of L1-CAM regulates axonal and dendritic bundling in vitro. *European Journal of Neuroscience*. https://doi.org/10.1111/j.1460-9568.2010.07447.x

Barstead, R., Moulder, G., Cobb, B., Frazee, S., Henthorn, D., Holmes, J., Jerebie, D., Landsdale, M., Osborn, J., Pritchett, C., Robertson, J., Rummage, J., Stokes, E., Vishwanathan, M., Mitani, S., Gengyo-Ando, K., Funatsu, O., Hori, S., Imae, R., … Zapf, R. (2012). Large-scale screening for targeted knockouts in the caenorhabditis elegans genome. *G3: Genes, Genomes, Genetics*. https://doi.org/10.1534/g3.112.003830

Boyle, T. J., Bao, Z., Murray, J. I., Araya, C. L., & Waterston, R. H. (2006). AceTree: A tool for visual analysis of Caenorhabditis elegans embryogenesis. *BMC Bioinformatics*. https://doi.org/10.1186/1471-2105-7-275

Brittin, C. A., Cook, S. J., Hall, D. H., & Emmons, S. W. (2020). Beyond the connectome : A map of a brain architecture derived from whole-brain volumetric reconstructions. *BioRxiv*.

Brittin, C., Cook, S., Hall, D., Emmons, S., & Cohen, N. (2018). Volumetric

reconstruction of main Caenorhabditis elegans neuropil at two different time points. *BioRxiv*. https://doi.org/10.1101/485771

Chalasani, S. H., Chronis, N., Tsunozaki, M., Gray, J. M., Ramot, D., Goodman, M. B., & Bargmann, C. I. (2007). Dissecting a circuit for olfactory behaviour in Caenorhabditis elegans. *Nature*. https://doi.org/10.1038/nature06292

Chelur, D. S., & Chalfie, M. (2007). Targeted cell killing by reconstituted caspases. *Proceedings of the National Academy of Sciences of the United States of America*. https://doi.org/10.1073/pnas.0610877104

Christensen, R., de la Torre-Ubieta, L., Bonni, A., & Colón-Ramos, D. A. (2011). A conserved PTEN/FOXO pathway regulates neuronal morphology during C. elegans development. *Development*, *138*(23), 5257 LP – 5267. https://doi.org/10.1242/dev.069062

Clandinin, T. R., & Feldheim, D. A. (2009). Making a visual map: mechanisms and molecules. In *Current Opinion in Neurobiology*. https://doi.org/10.1016/j.conb.2009.04.011

Cook, S. J., Jarrell, T. A., Brittin, C. A., Wang, Y., Bloniarz, A. E., Yakovlev, M. A., Nguyen, K. C. Q., Tang, L. T. H., Bayer, E. A., Duerr, J. S., Bülow, H. E., Hobert, O., Hall, D. H., & Emmons, S. W. (2019). Whole-animal connectomes of both Caenorhabditis elegans sexes. *Nature*. https://doi.org/10.1038/s41586-019-1352-7

Davis, M. W., Hammarlund, M., Harrach, T., Hullett, P., Olsen, S., & Jorgensen, E. M. (2005). Rapid single nucleotide polymophism mapping in C. elegans. *BMC Genomics*. https://doi.org/10.1186/1471-2164-6-118

Demb, J. B., & Singer, J. H. (2012). Intrinsic properties and functional circuitry of the AII amacrine cell. In *Visual Neuroscience*. https://doi.org/10.1017/S0952523811000368

Duncan, L. H., Moyle, M. W., Shao, L., Sengupta, T., Ikegami, R., Kumar, A., Guo, M., Christensen, R., Santella, A., Bao, Z., Shroff, H., Mohler, W., & Colón-Ramos, D. A. (2019). Isotropic light-sheet microscopy and automated

cell lineage analyses to catalogue caenorhabditis elegans embryogenesis with subcellular resolution. *Journal of Visualized Experiments*. https://doi.org/10.3791/59533

Fan, J., Ji, T., Wang, K., Huang, J., Wang, M., Manning, L., Dong, X., Shi, Y., Zhang, X., Shao, Z., & Colón-Ramos, D. A. (2020). A muscle-epidermis-glia signaling axis sustains synaptic specificity during allometric growth in caenorhabditis elegans. *ELife*. https://doi.org/10.7554/eLife.55890

Foty, R. A., & Steinberg, M. S. (2005). The differential adhesion hypothesis: A direct evaluation. *Developmental Biology*. https://doi.org/10.1016/j.ydbio.2004.11.012

Foty, R. A., & Steinberg, M. S. (2013). Differential adhesion in model systems. In *Wiley interdisciplinary reviews. Developmental biology*. https://doi.org/10.1002/wdev.104

Gabriel, J. P., Trivedi, C. A., Maurer, C. M., Ryu, S., & Bollmann, J. H. (2012). Layer-Specific Targeting of Direction-Selective Neurons in the Zebrafish Optic Tectum. *Neuron*, *76*(6), 1147–1160. https://doi.org/https://doi.org/10.1016/j.neuron.2012.12.003

Garg, P., Verma, R., Nihalani, D., Johnstone, D. B., & Holzman, L. B. (2007). Neph1 Cooperates with Nephrin To Transduce a Signal That Induces Actin Polymerization. *Molecular and Cellular Biology*. https://doi.org/10.1128/mcb.00948-07

Gray, J. M., Hill, J. J., & Bargmann, C. I. (2005). A circuit for navigation in Caenorhabditis elegans. *Proceedings of the National Academy of Sciences of the United States of America*. https://doi.org/10.1073/pnas.0409009101

Grossman, E. N., Giurumescu, C. A., & Chisholm, A. D. (2013). Mechanisms of ephrin receptor protein kinase-independent signaling in amphid axon guidance in Caenorhabditis elegans. *Genetics*. https://doi.org/10.1534/genetics.113.154393

Han, J., Kamber, M., & Pei, J. (2012). Data Mining: Concepts and Techniques. In

Data Mining: Concepts and Techniques. https://doi.org/10.1016/C2009-0-61819-5

Hong, R. L., Riebesell, M., Bumbarger, D. J., Cook, S. J., Carstensen, H. R., Sarpolaki, T., Cochella, L., Castrejon, J., Moreno, E., Sieriebriennikov, B., Hobert, O., & Sommer, R. J. (2019). Evolution of neuronal anatomy and circuitry in two highly divergent nematode species. *ELife*. https://doi.org/10.7554/eLife.47155

Honig, M. G., Frase, P. A., & Camilli, S. J. (1998). The spatial relationships among cutaneous, muscle sensory and motoneuron axone during development of the chick hindlimb. *Development*.

Kang, C., & Avery, L. (2009). Systemic regulation of starvation response in Caenorhabditis elegans. *Genes and Development*. https://doi.org/10.1101/gad.1723409

Kim, J. H., Ren, Y., Ng, W. P., Li, S., Son, S., Kee, Y. S., Zhang, S., Zhang, G., Fletcher, D. A., Robinson, D. N., & Chen, E. H. (2015). Mechanical Tension Drives Cell Membrane Fusion. *Developmental Cell*. https://doi.org/10.1016/j.devcel.2015.01.005

Kolb, H. (1995). Roles of Amacrine Cells. In *Webvision: The Organization of the Retina and Visual System*.

Kolodkin, A. L., & Hiesinger, P. R. (2017). Wiring visual systems: common and divergent mechanisms and principles. In *Current Opinion in Neurobiology*. https://doi.org/10.1016/j.conb.2016.12.006

Kumar, A., Wu, Y., Christensen, R., Chandris, P., Gandler, W., McCreedy, E., Bokinsky, A., Colón-Ramos, D. A., Bao, Z., McAuliffe, M., Rondeau, G., & Shroff, H. (2014). Dual-view plane illumination microscopy for rapid and spatially isotropic imaging. *Nature Protocols*. https://doi.org/10.1038/nprot.2014.172

Kunzevitzky, N. J., Willeford, K. T., Feuer, W. J., Almeida, M. V., & Goldberg, J. L. (2013). Amacrine cell subtypes differ in their intrinsic neurite growth

capacity. *Investigative Ophthalmology and Visual Science*. https://doi.org/10.1167/iovs.13-12691

Lanjuin, A., VanHoven, M. K., Bargmann, C. I., Thompson, J. K., & Sengupta, P. (2003). Otx/otd homeobox genes specify distinct sensory neuron identities in C. elegans. *Developmental Cell*. https://doi.org/10.1016/S1534-5807(03)00293-4

Marc, R. E., Anderson, J. R., Jones, B. W., Sigulinsky, C. L., & Lauritzen, J. S. (2014). The All amacrine cell connectome: A dense network hub. *Frontiers in Neural Circuits*. https://doi.org/10.3389/fncir.2014.00104

Maynard, D. M. (1962). Organization of Neuropil. *Am. Zoologist*, *2*, 79–96.

Mello, C., & Fire, A. (1995). DNA Transformation. *Methods in Cell Biology*. https://doi.org/10.1016/S0091-679X(08)61399-0

Millard, S. S., & Pecot, M. Y. (2018). Strategies for assembling columns and layers in the Drosophila visual system. In *Neural Development*. https://doi.org/10.1186/s13064-018-0106-9

Minevich, G., Park, D. S., Blankenberg, D., Poole, R. J., & Hobert, O. (2012). CloudMap: A cloud-based pipeline for analysis of mutant genome sequences. *Genetics*. https://doi.org/10.1534/genetics.112.144204

Moyle, M. W., Barnes, K. M., Kuchroo, M., Gonopolskiy, A., Duncan, L. H., Sengupta, T., Shao, L., Guo, M., Santella, A., Christensen, R., Kumar, A., Wu, Y., Moon, K. R., Wolf, G., Krishnaswamy, S., Bao, Z., Shroff, H., Mohler, W., & Colón-Ramos, D. A. (2020). Structural and developmental principles of neuropil assembly in C. elegans *BioRxiv*, 2020.03.15.992222. https://doi.org/10.1101/2020.03.15.992222

Murray, J. I., Bao, Z., Boyle, T. J., & Waterston, R. H. (2006). The lineaging of fluorescently-labeled Caenorhabditis elegans embryos with StarryNite and AceTree. *Nature Protocols*. https://doi.org/10.1038/nprot.2006.222

Nevin, L. M., Taylor, M. R., & Baier, H. (2008). Hardwiring of fine synaptic layers in the zebrafish visual pathway. *Neural Development*.

https://doi.org/10.1186/1749-8104-3-36

Petrovic, M., & Hummel, T. (2008a). Temporal identity in axonal target layer recognition. *Nature*. https://doi.org/10.1038/nature07407

Petrovic, M., & Hummel, T. (2008b). Temporal identity in axonal target layer recognition. *Nature*. https://doi.org/10.1038/nature07407

Piggott, B. J., Liu, J., Feng, Z., Wescott, S. A., & Xu, X. Z. S. (2011). The neural circuits and synaptic mechanisms underlying motor initiation in C. elegans. *Cell*. https://doi.org/10.1016/j.cell.2011.08.053

Poskanzer, K., Needleman, L. A., Bozdagi, O., & Huntley, G. W. (2003). N-cadherin regulates ingrowth and laminar targeting of thalamocortical axons. *The Journal of Neuroscience : The Official Journal of the Society for Neuroscience*.

Robles, E., Filosa, A., & Baier, H. (2013). Precise lamination of retinal axons generates multiple parallel input pathways in the tectum. *Journal of Neuroscience*. https://doi.org/10.1523/JNEUROSCI.4990-12.2013

Robles, E., Smith, S. J., & Baier, H. (2011). Characterization of genetically targeted neuron types in the zebrafish optic tectum. *Frontiers in Neural Circuits*. https://doi.org/10.3389/fncir.2011.00001

Rubinov, M., & Sporns, O. (2010). Complex network measures of brain connectivity: Uses and interpretations. *NeuroImage*. https://doi.org/10.1016/j.neuroimage.2009.10.003

Sabrin, K., Wei, Y., van den Heuvel, M., & Dovrolis, C. (2019). The hourglass organization of the Caenorhabditis elegans connectome. *BioRxiv*. https://doi.org/10.1101/600999

Sanes, J. R., & Zipursky, S. L. (2010). Design Principles of Insect and Vertebrate Visual Systems. In *Neuron*. https://doi.org/10.1016/j.neuron.2010.01.018

Sanes, J. R., & Zipursky, S. L. (2020). Synaptic Specificity, Recognition Molecules, and Assembly of Neural Circuits. In *Cell*. https://doi.org/10.1016/j.cell.2020.04.008

1383 Santella, A., Du, Z., & Bao, Z. (2014). A semi-local neighborhood-based
1384 framework for probabilistic cell lineage tracing. *BMC Bioinformatics*.
1385 https://doi.org/10.1186/1471-2105-15-217
1386 Sarin, S., Prabhu, S., O'Meara, M. M., Pe'er, I., & Hobert, O. (2008).
1387 Caenorhabditis elegans mutant allele identification by whole-genome
1388 sequencing. *Nature Methods*. https://doi.org/10.1038/nmeth.1249
1389 Schindelin, J., Arganda-Carreras, I., Frise, E., Kaynig, V., Longair, M., Pietzsch,
1390 T., Preibisch, S., Rueden, C., Saalfeld, S., Schmid, B., Tinevez, J. Y., White,
1391 D. J., Hartenstein, V., Eliceiri, K., Tomancak, P., & Cardona, A. (2012). Fiji:
1392 An open-source platform for biological-image analysis. In *Nature Methods*.
1393 https://doi.org/10.1038/nmeth.2019
1394 Schürmann, F. W. (2016). Fine structure of synaptic sites and circuits in
1395 mushroom bodies of insect brains. In *Arthropod Structure and Development*.
1396 https://doi.org/10.1016/j.asd.2016.08.005
1397 Schwabe, T., Borycz, J. A., Meinertzhagen, I. A., & Clandinin, T. R. (2014).
1398 Differential adhesion determines the organization of synaptic fascicles in the
1399 drosophila visual system. *Current Biology*.
1400 https://doi.org/10.1016/j.cub.2014.04.047
1401 Schwarz, V., Pan, J., Voltmer-Irsch, S., & Hutter, H. (2009). IgCAMs redundantly
1402 control axon navigation in Caenorhabditis elegans. *Neural Development*.
1403 https://doi.org/10.1186/1749-8104-4-13
1404 Serizawa, S., Miyamichi, K., Takeuchi, H., Yamagishi, Y., Suzuki, M., & Sakano,
1405 H. (2006). A Neuronal Identity Code for the Odorant Receptor-Specific and
1406 Activity-Dependent Axon Sorting. *Cell*.
1407 https://doi.org/10.1016/j.cell.2006.10.031
1408 Shen, K., & Bargmann, C. I. (2003). The immunoglobulin superfamily protein
1409 SYG-1 determines the location of specific synapses in C. elegans. *Cell*.
1410 https://doi.org/10.1016/S0092-8674(03)00113-2
1411 Shen, K., Fetter, R. D., & Bargmann, C. I. (2004). Synaptic specificity is

generated by the synaptic guidepost protein SYG-2 and its receptor, SYG-1. *Cell*. https://doi.org/10.1016/S0092-8674(04)00251-X

Šmít, D., Fouquet, C., Pincet, F., Zapotocky, M., & Trembleau, A. (2017). Axon tension regulates fasciculation/defasciculation through the control of axon shaft zippering. *ELife*. https://doi.org/10.7554/eLife.19907

Soiza-Reilly, M., & Commons, K. G. (2014). Unraveling the architecture of the dorsal raphe synaptic neuropil using high-resolution neuroanatomy. In *Frontiers in Neural Circuits*. https://doi.org/10.3389/fncir.2014.00105

Steinberg, M. S. (1962). Mechanism of tissue reconstruction by dissociated cells, II: Time-course of events. *Science*. https://doi.org/10.1126/science.137.3532.762

Strettoi, E., Raviola, E., & Dacheux, R. F. (1992). Synaptic connections of the narrow-field, bistratified rod amacrine cell (AII) in the rabbit retina. *Journal of Comparative Neurology*. https://doi.org/10.1002/cne.903250203

Tan, L., Zhang, K. X., Pecot, M. Y., Nagarkar-Jaiswal, S., Lee, P. T., Takemura, S. Y., McEwen, J. M., Nern, A., Xu, S., Tadros, W., Chen, Z., Zinn, K., Bellen, H. J., Morey, M., & Zipursky, S. L. (2015). Ig Superfamily Ligand and Receptor Pairs Expressed in Synaptic Partners in Drosophila. *Cell*. https://doi.org/10.1016/j.cell.2015.11.021

Taylor, W. R., & Smith, R. G. (2012). The role of starburst amacrine cells in visual signal processing. *Visual Neuroscience*. https://doi.org/10.1017/S0952523811000393

Towlson, E. K., Vértes, P. E., Ahnert, S. E., Schafer, W. R., & Bullmore, E. T. (2013). The rich club of the C. elegans neuronal connectome. *Journal of Neuroscience*. https://doi.org/10.1523/JNEUROSCI.3784-12.2013

Voyiadjis, A. G., Doumi, M., Curcio, E., & Shinbrot, T. (2011). Fasciculation and defasciculation of neurite bundles on micropatterned substrates. *Annals of Biomedical Engineering*. https://doi.org/10.1007/s10439-010-0168-2

Wakabayashi, T., Kitagawa, I., & Shingai, R. (2004). Neurons regulating the

duration of forward locomotion in Caenorhabditis elegans. *Neuroscience Research*. https://doi.org/10.1016/j.neures.2004.06.005

Walton, T., Preston, E., Nair, G., Zacharias, A. L., Raj, A., & Murray, J. I. (2015). The Bicoid Class Homeodomain Factors ceh-36/OTX and unc-30/PITX Cooperate in C. elegans Embryonic Progenitor Cells to Regulate Robust Development. *PLoS Genetics*. https://doi.org/10.1371/journal.pgen.1005003

Ware, R. W., Clark, D., Crossland, K., & Russell, R. L. (1975). The nerve ring of the nematode Caenorhabditis elegans: Sensory input and motor output. *Journal of Comparative Neurology*. https://doi.org/10.1002/cne.901620106

Weigert, M., Schmidt, U., Boothe, T., Müller, A., Dibrov, A., Jain, A., Wilhelm, B., Schmidt, D., Broaddus, C., Culley, S., Rocha-Martins, M., Segovia-Miranda, F., Norden, C., Henriques, R., Zerial, M., Solimena, M., Rink, J., Tomancak, P., Royer, L., … Myers, E. W. (2018). Content-aware image restoration: pushing the limits of fluorescence microscopy. *Nature Methods*. https://doi.org/10.1038/s41592-018-0216-7

White, J. G., Southgate, E., Thomson, J. N., & Brenner, S. (1983). Factors that determine connectivity in the nervous system of Caenorhabditis elegans. *Cold Spring Harbor Symposia on Quantitative Biology*. https://doi.org/10.1101/sqb.1983.048.01.067

White, J. G., Southgate, E., Thomson, J. N., & Brenner, S. (1986). The structure of the nervous system of the nematode C. elegans. *Philosophical Transactions of the Royal Society of London - Series B: Biological Sciences*.

Witvliet, D., Mulcahy, B., Mitchell, J. K., Meirovitch, Y., Berger, D. R., Wu, Y., Liu, Y., Koh, W. X., Parvathala, R., Holmyard, D., Schalek, R. L., Shavit, N., Chisholm, A. D., Lichtman, J. W., Samuel, A. D. T., & Zhen, M. (2020). Connectomes across development reveal principles of brain maturation in C. elegans *BioRxiv*, 2020.04.30.066209. https://doi.org/10.1101/2020.04.30.066209

Wu, Y., Chandris, P., Winter, P. W., Kim, E. Y., Jaumouillé, V., Kumar, A., Guo,

M., Leung, J. M., Smith, C., Rey-Suarez, I., Liu, H., Waterman, C. M., Ramamurthi, K. S., La Riviere, P. J., & Shroff, H. (2016). Simultaneous multiview capture and fusion improves spatial resolution in wide-field and light-sheet microscopy. *Optica*. https://doi.org/10.1364/optica.3.000897

Wu, Y., Wawrzusin, P., Senseney, J., Fischer, R. S., Christensen, R., Santella, A., York, A. G., Winter, P. W., Waterman, C. M., Bao, Z., Colón-Ramos, D. A., McAuliffe, M., & Shroff, H. (2013). Spatially isotropic four-dimensional imaging with dual-view plane illumination microscopy. *Nature Biotechnology*. https://doi.org/10.1038/nbt.2713

Xu, C. S., Januszewski, M., Lu, Z., Takemura, S., Hayworth, K. J., Huang, G., Shinomiya, K., Maitin-Shepard, J., Ackerman, D., Berg, S., Blakely, T., Bogovic, J., Clements, J., Dolafi, T., Hubbard, P., Kainmueller, D., Katz, W., Kawase, T., Khairy, K. A., … Plaza, S. M. (2020). A Connectome of the Adult Drosophila Central Brain. *BioRxiv*, 2020.01.21.911859. https://doi.org/10.1101/2020.01.21.911859

Xuan, Z., Manning, L., Nelson, J., Richmond, J. E., Colón-Ramos, D. A., Shen, K., & Kurshan, P. T. (2017). Clarinet (CLA-1), a novel active zone protein required for synaptic vesicle clustering and release. *ELife*. https://doi.org/10.7554/eLife.29276

Yamagata, M., & Sanes, J. R. (2008). Dscam and Sidekick proteins direct lamina-specific synaptic connections in vertebrate retina. *Nature*. https://doi.org/10.1038/nature06469

Yamagata, M., & Sanes, J. R. (2012). Expanding the Ig superfamily code for laminar specificity in retina: Expression and role of contactins. *Journal of Neuroscience*. https://doi.org/10.1523/JNEUROSCI.3193-12.2012

Yoshimura, S., Murray, J. I., Lu, Y., Waterston, R. H., & Shaham, S. (2008). mls-2 and vab-3 control glia development, hlh-17/Olig expression and glia-dependent neurite extension in C. elegans

Development, *135*(13), 2263 LP – 2275. https://doi.org/10.1242/dev.019547

Zallen, J. A., Kirch, S. A., & Bargmann, C. I. (1999). Genes required for axon pathfinding and extension in the C. elegans nerve ring. *Development*.

Zhen, M., & Jin, Y. (1999). The liprin protein SYD-2 regulates the differentiation of presynaptic termini in C. elegans. *Nature*. https://doi.org/10.1038/43886

Zheng, Z., Lauritzen, J. S., Perlman, E., Robinson, C. G., Nichols, M., Milkie, D., Torrens, O., Price, J., Fisher, C. B., Sharifi, N., Calle-Schuler, S. A., Kmecova, L., Ali, I. J., Karsh, B., Trautman, E. T., Bogovic, J. A., Hanslovsky, P., Jefferis, G. S. X. E., Kazhdan, M., … Bock, D. D. (2018). A Complete Electron Microscopy Volume of the Brain of Adult Drosophila melanogaster. *Cell*, *174*(3), 730-743.e22. https://doi.org/10.1016/j.cell.2018.06.019

ztokatli, H. Ö., Hörnberg, M., Berghard, A., & Bohm, S. (2012). Retinoic acid receptor and CNGA2 channel signaling are part of a regulatory feedback loop controlling axonal convergence and survival of olfactory sensory neurons. *The FASEB Journal*. https://doi.org/10.1096/fj.11-192450

Figure 1

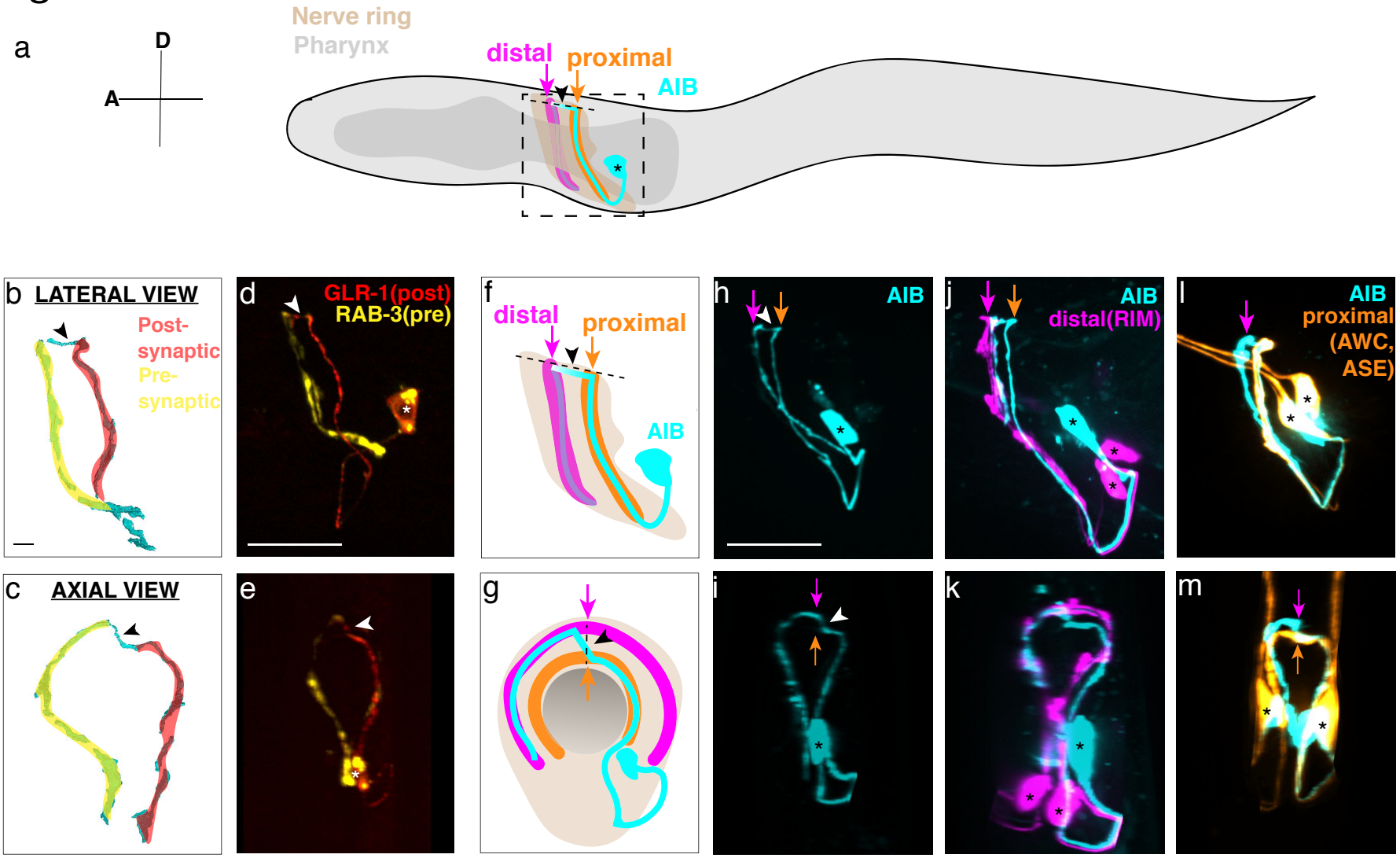

Figure 2

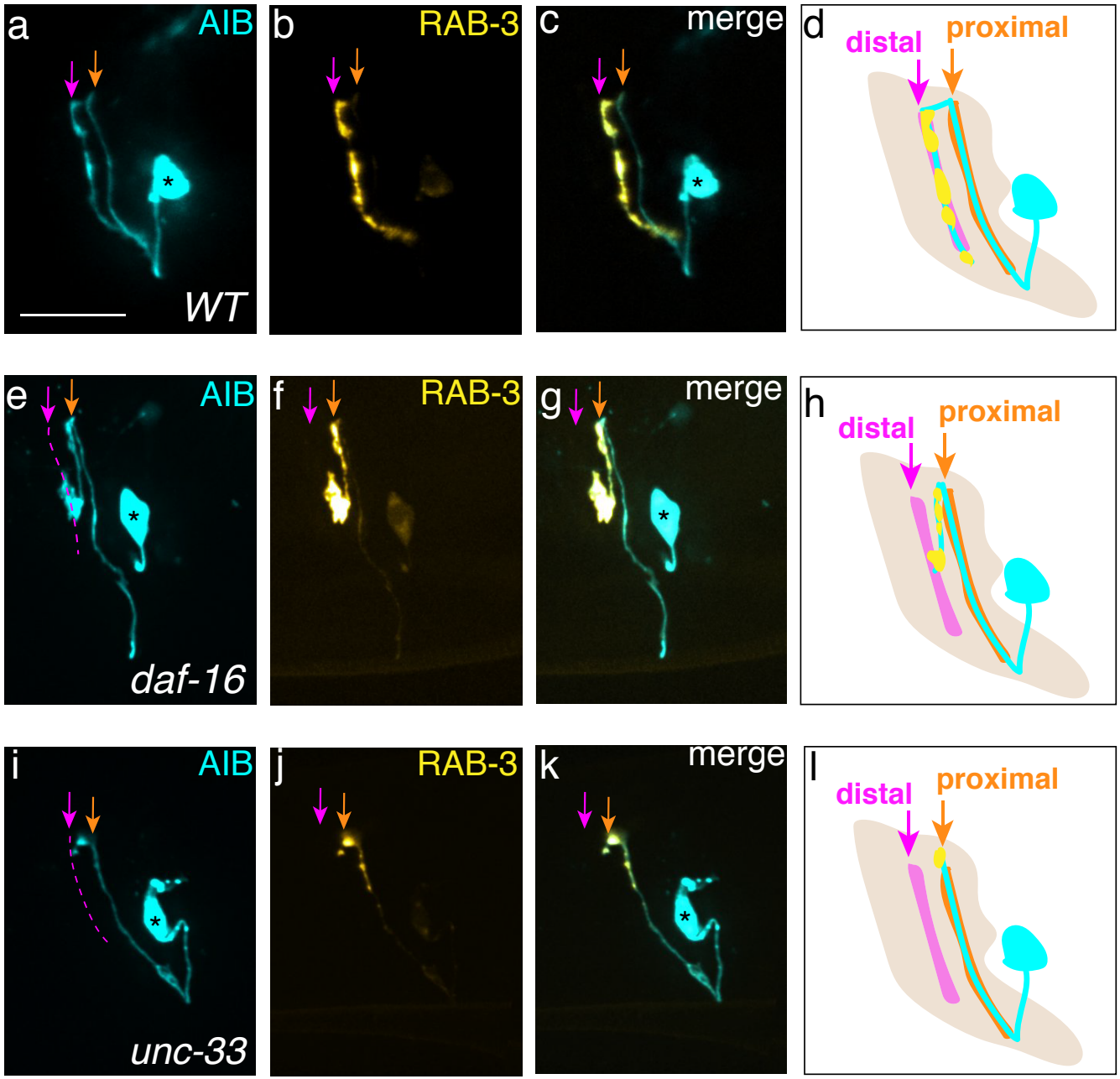

Figure 3

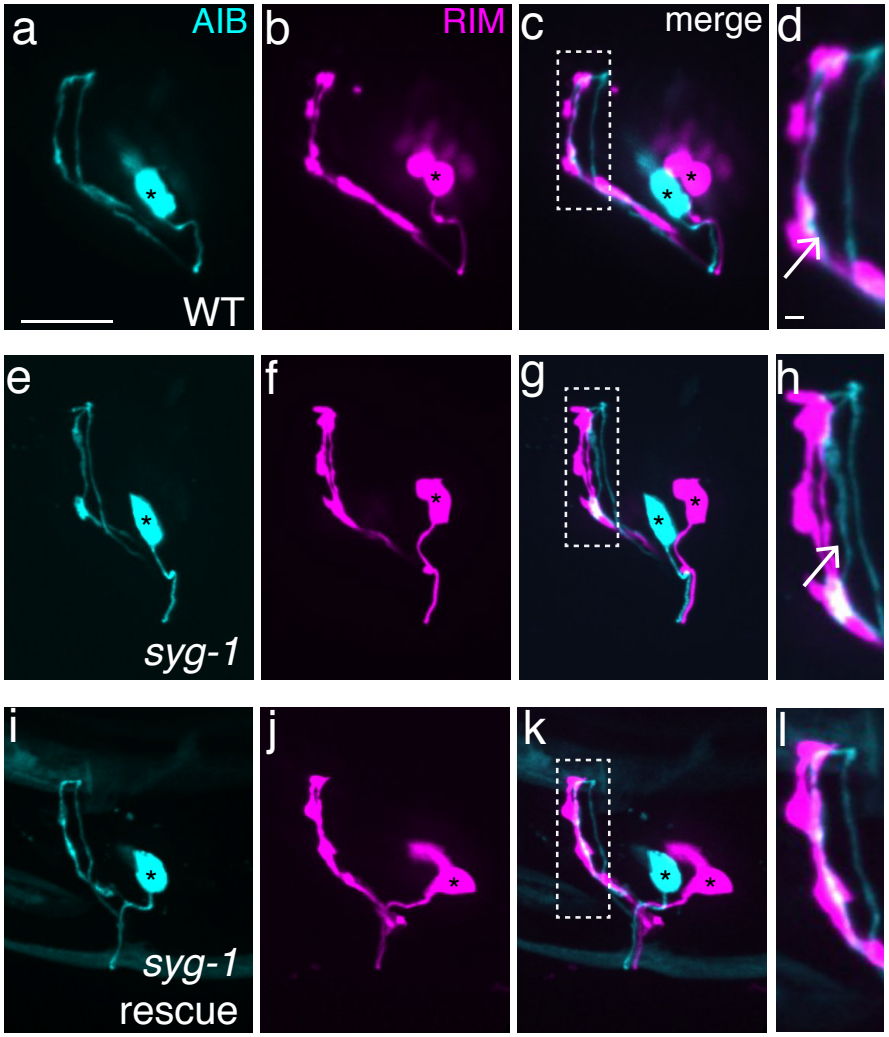

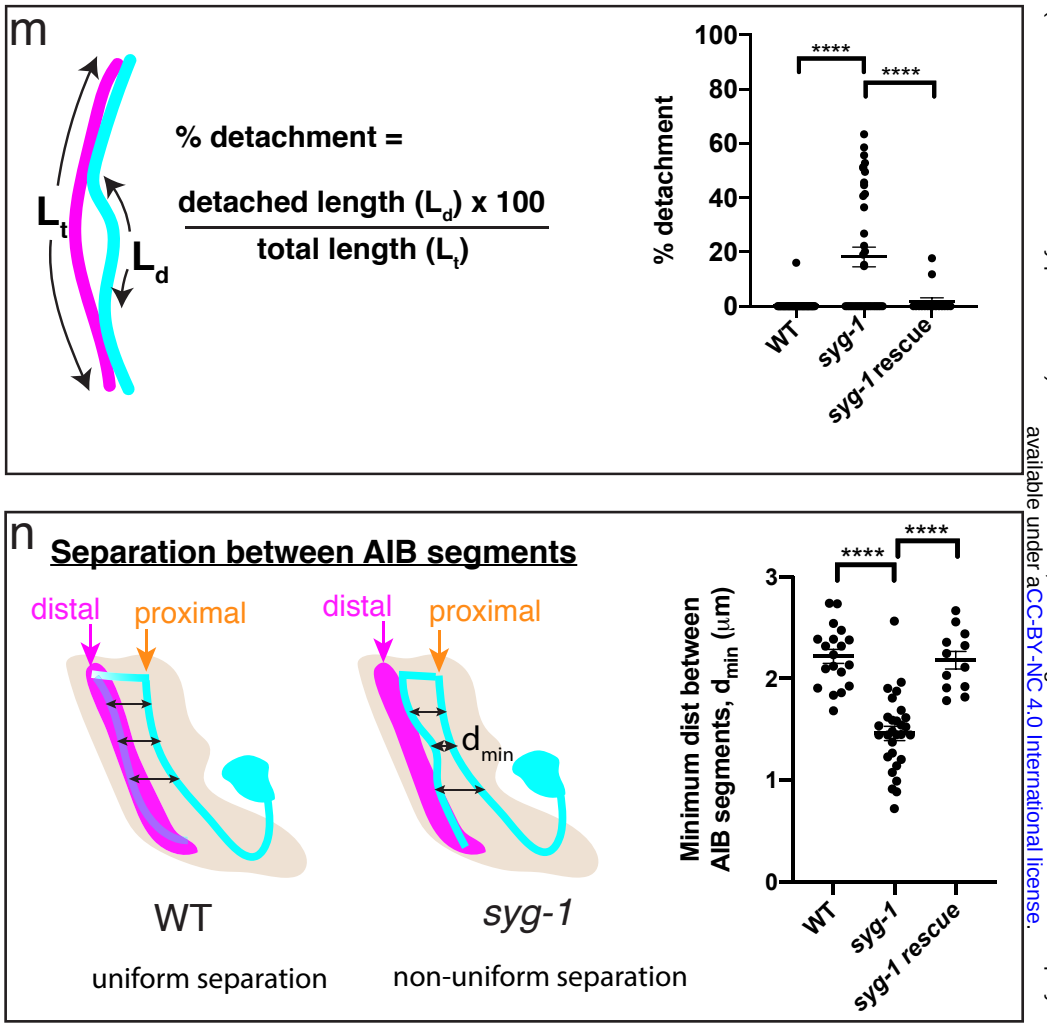

Figure 4

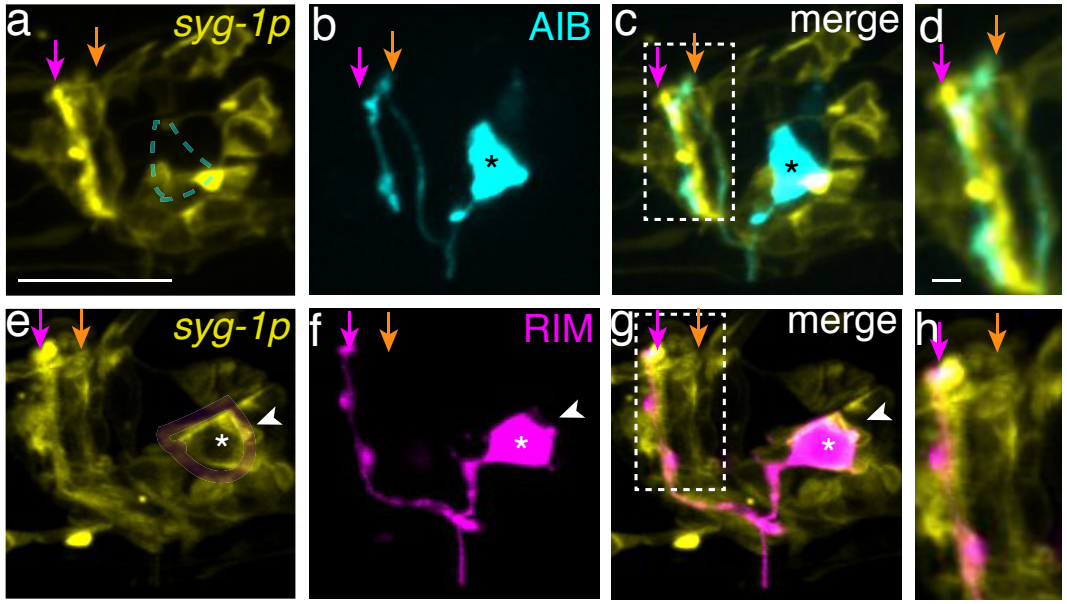

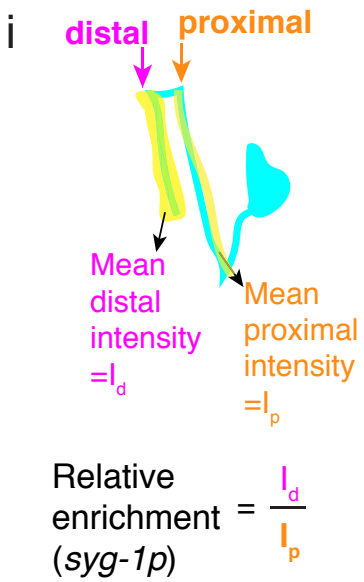

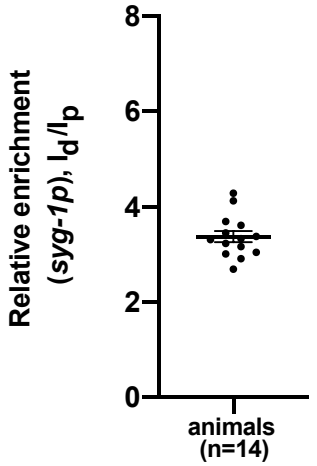

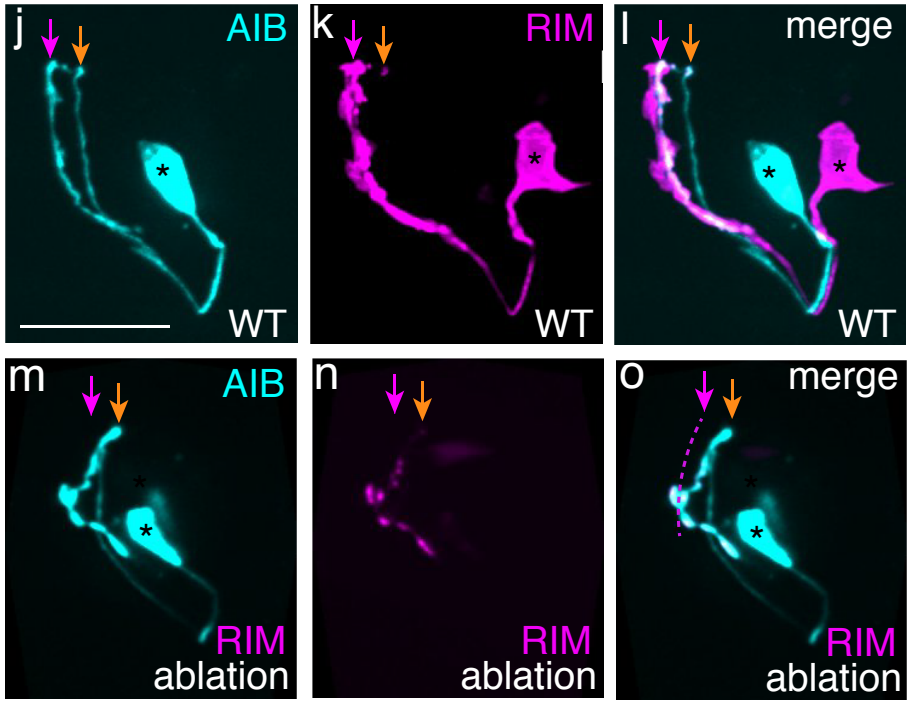

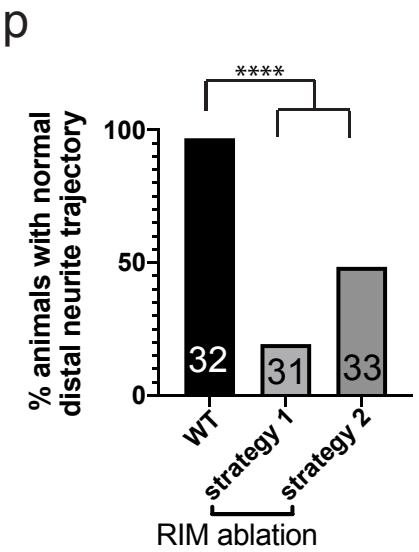

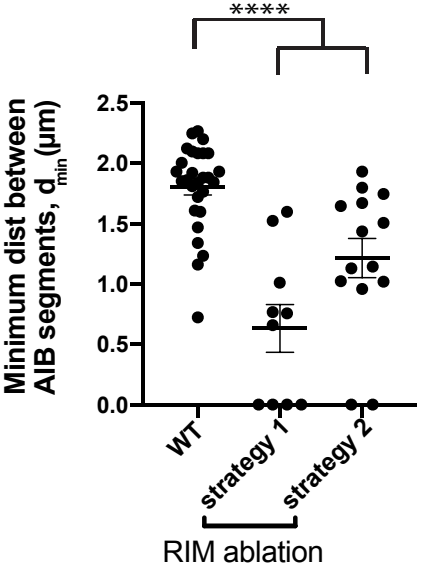

Figure 5

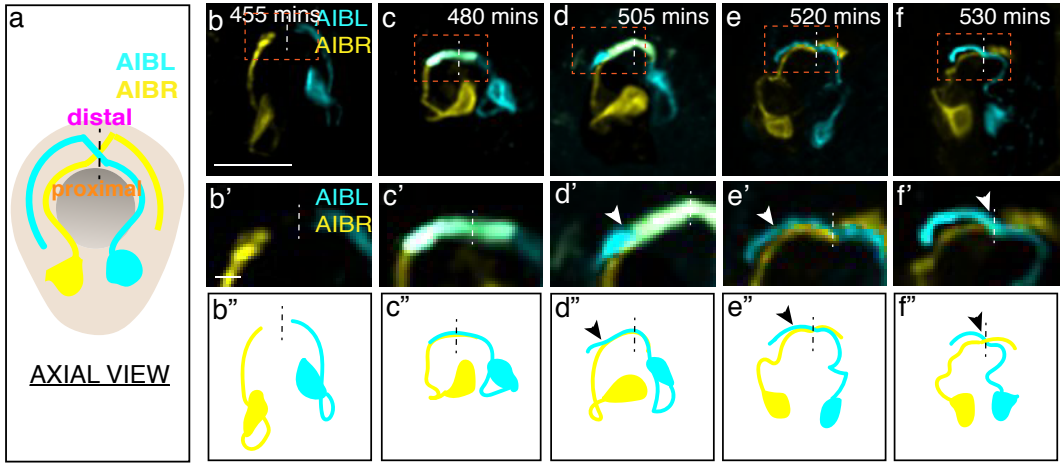

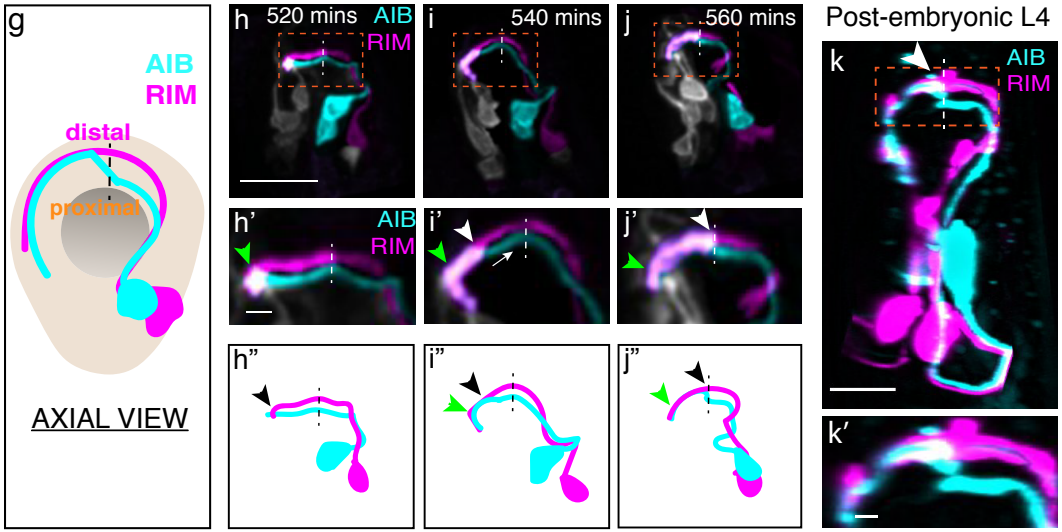

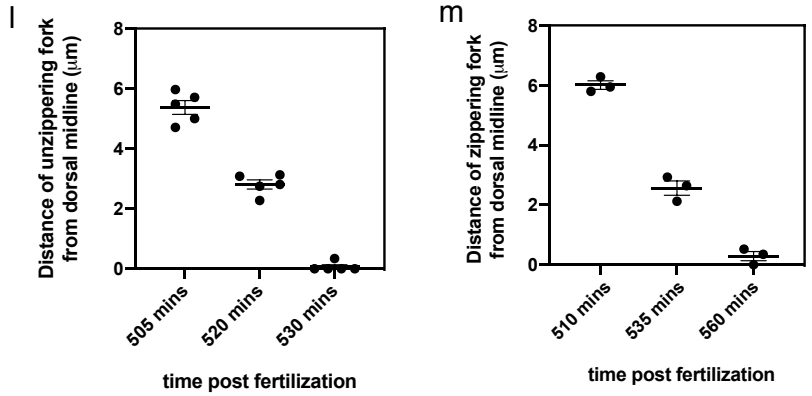

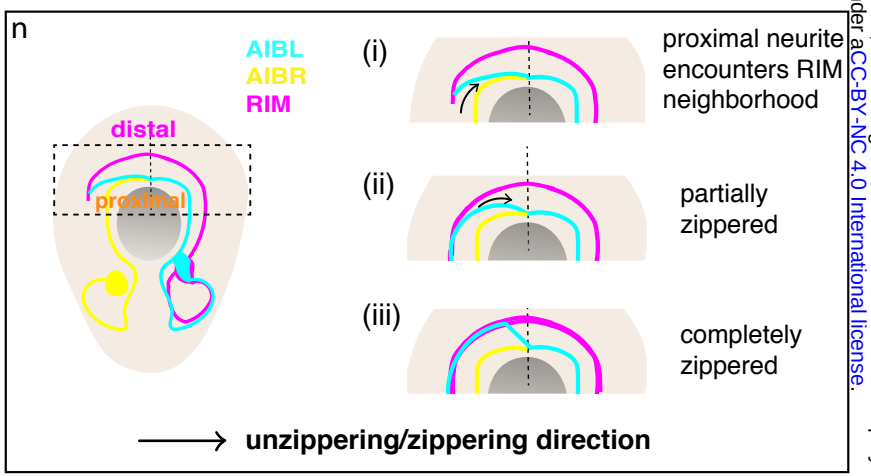

Figure 6

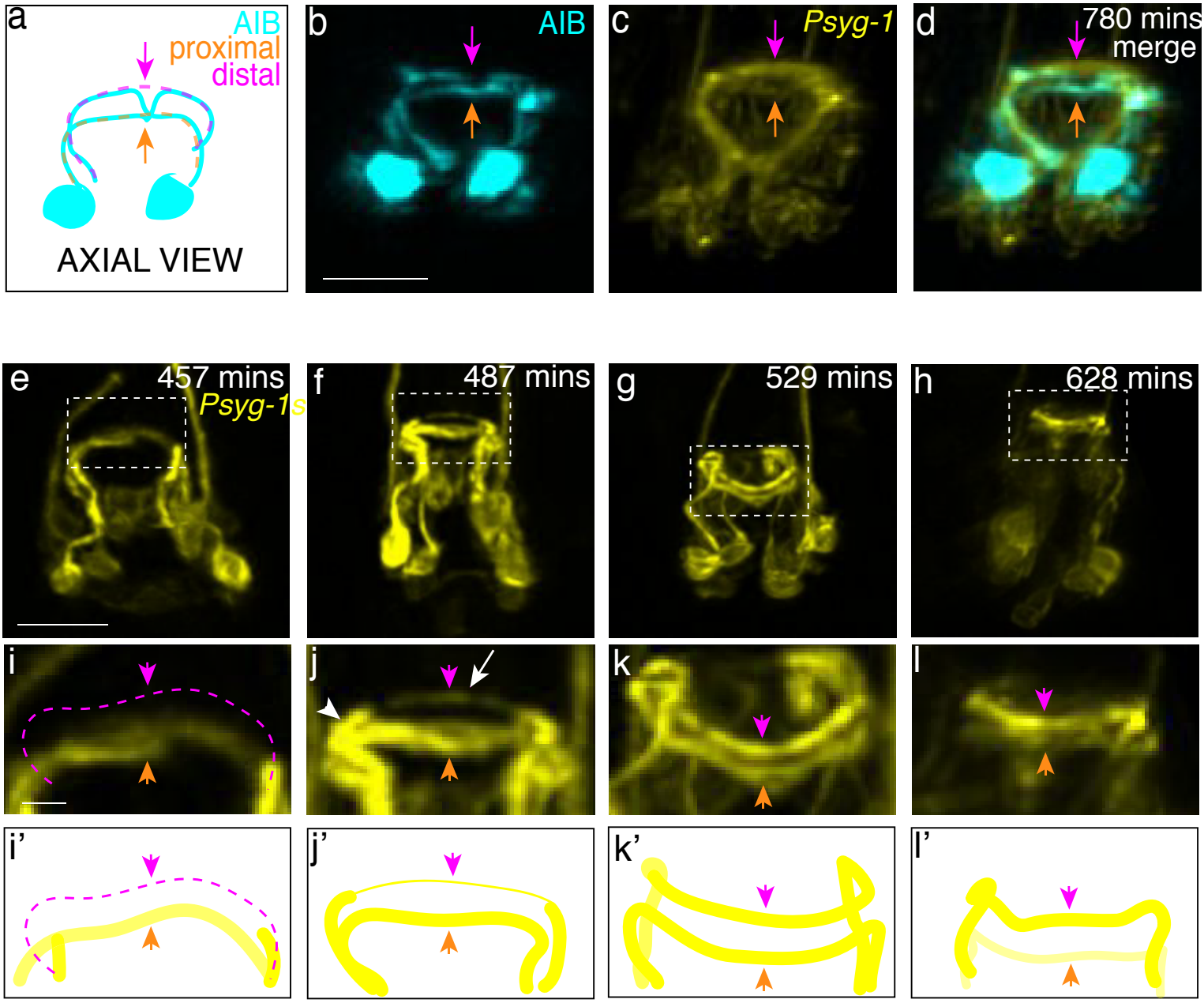

Figure 7

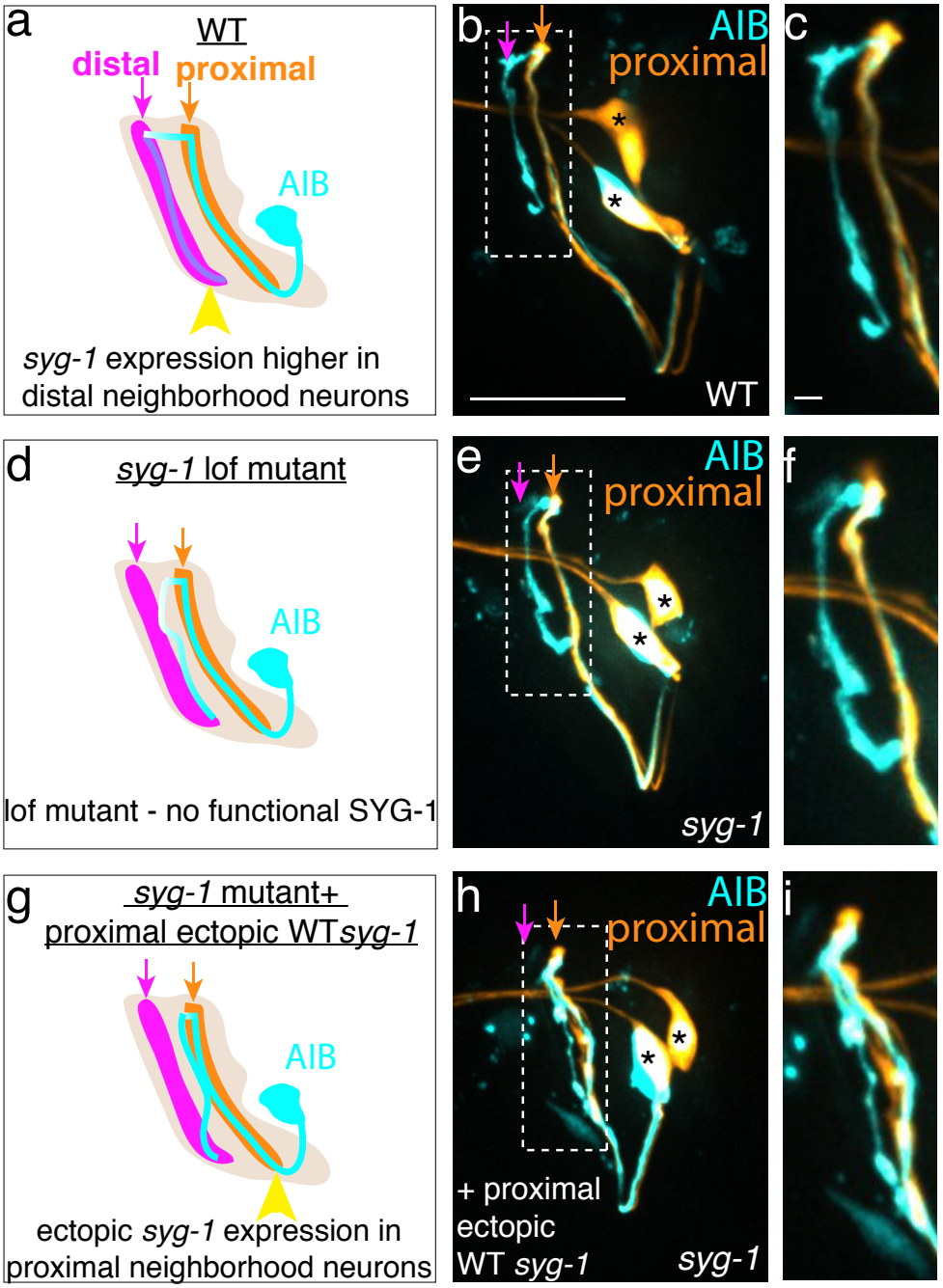

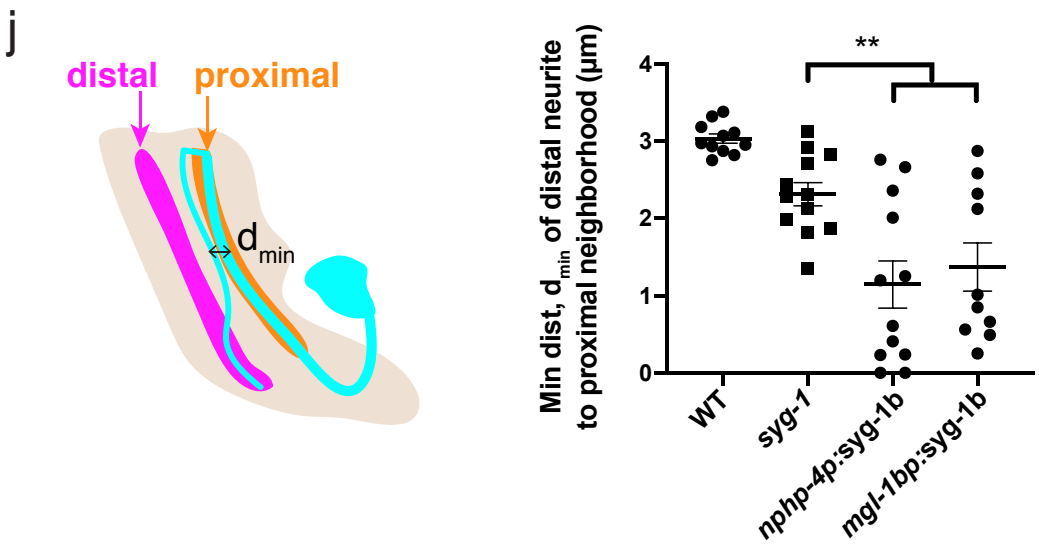

Figure 8